Four-point Bending Based Low-Carbon Steel Plate Corrosion Monitoring by Optical Fiber Bragg Grating Strain Sensor

by

Zihao Zhong

Bachelor of Science in Physics, Nanjing University, 2017

Submitted to the Graduate Faculty of

Swanson School of Engineering in partial fulfillment

of the requirements for the degree of

Master of Science in Mechanical Engineering

University of Pittsburgh

2019

UNIVERSITY OF PITTSBURGH

SWANSON SCHOOL OF ENGINEERING

This thesis was presented

by

Zihao Zhong

It was defended on

July 12, 2019

and approved by

Qing-Ming Wang, Ph.D., Professor
Department of Mechanical Engineering and Materials Science

Heng Ban, Ph.D., Professor
Department of Mechanical Engineering and Materials Science

Patrick Smolinski, Ph.D., Associate Professor
Department of Mechanical Engineering and Materials Science

Thesis Advisor: Qing-Ming Wang, Ph.D., Professor
Department of Mechanical Engineering and Materials Science

Four-point Bending Based Low-Carbon Steel Plate Corrosion Monitoring by Optical Fiber Bragg Grating Strain Sensor

Zihao Zhong, M.S.

University of Pittsburgh, 2019

Fiber Bragg Grating (FBG) Sensor is very sensible to strain change, with 1.2 pm shift in Bragg wavelength when suffering 1 μm strain change [1]. Metal corrosion is big problem in our world. In order to monitor this process, many methods are proposed, but seldom focus on the strain change of metal plate during corrosion. One reason for this is that the strain change during corrosion is much smaller than the sensitivities of most sensors. Another problem is the residual strain left in metal products, which will also be released during corrosion without an obvious regularity. Our solution is applying a bending to the metal plate, keeping curvature radius at the medium of the metal plate unchanged during corrosion. As to the residual strain, which has a non-negligible influence in order of magnitudes, we set another metal plate made in same process without bending. By comparing the results of the bent and unbent plates, the strain changes only contributed by the bending during corrosion can be achieved. We calculate a model to analyze the strain changes contributed by bending during corrosion. The expected result is that the rate of strain change during corrosion is always in positive correlation with the corrosion speed. After 500 hours corrosion experiment, the low-carbon steel (0.13-0.20% Carbon) plate with 1.59 mm in thickness at the beginning corroded $0.1202 \pm 0.0088\text{mm}$, and the total strain change contributed by bending is $91.213 \pm 3.158\mu\varepsilon$. Strain transfer rate is1.4759 ± 0.0026, and the strain loss due to the adhesive layer is $32.24\% \pm 0.16\%$. The rate of strain change during corrosion for the results is positive during corrosion, fitting the expectation very well. The sensitivity for AQ6374 is 0.002nm, and the corresponding sensitivity for strain on FBG is $1.67 \pm 0.01\mu\varepsilon$. After considering the strain loss, the sensitivity for host material (carbon steel plate) is $2.46 \pm 0.03\mu\varepsilon$.

Table of Contents

List of Tables

List of Figures

Preface

As a guy with bachelor's degree with major in Physics, the day I spent as a graduate student in the department of engineering in the University of Pittsburgh is very challenging and meaningful for me.

Above all, I am very grateful to my advisor, Dr. Qing-Ming Wang, who is extremely patient, keen and professional whenever I encounter difficulties. After 4 years learning in Physics in Nanjing University in China, I have developed good ability in theory study. However, the lack of experiment experience is a big short lab for me. Fortunately, Dr. Wang always gives me decent advice to overcome every difficulty and another chance to try it again.

What's more, I am also grateful to my laboratory members, Qiuyan Li, Xueqi Li and Peiyuan Hsiao for their experience sharing and discussions on experimental design. I still remember the day that I just entered Dr. Wang's lab, I faced the huge break between theory and practice. I never know there are so many tips in actual use when it comes to artificial processing and operate machines. I am highly appreciated that their advice and help on my research turn out to be crucial to my success of this research.

I would like to express my thanks formally to my parents. They not only support me financially but also answer my doubts about life and academia.

1.0 Introduction

Optic Fiber Sensors (OFSs), specially Fiber Bragg Grating (FBG) sensors, have been highlighted in recent years, turning into several practical measurement methods and monitoring system [2]–[6]. Several physical properties have been successfully measured and monitored by these sensors, such as temperature, strain, pressure, voltage, refractive of index and so on [7]–[12]. As shown in Figure 1, FBG has a periodic variation in the refractive index of the fiber core, usually 1mm to 10mm in length, making the Bragg Diffraction possible in its longitudinal direction within the fiber. Such structure can reflect a certain narrow band of light, which is closely connected to the distance between the gratings. In this way, any physical properties that can cause the distance between gratings changing in a regular way, can be measured by FBG sensor.

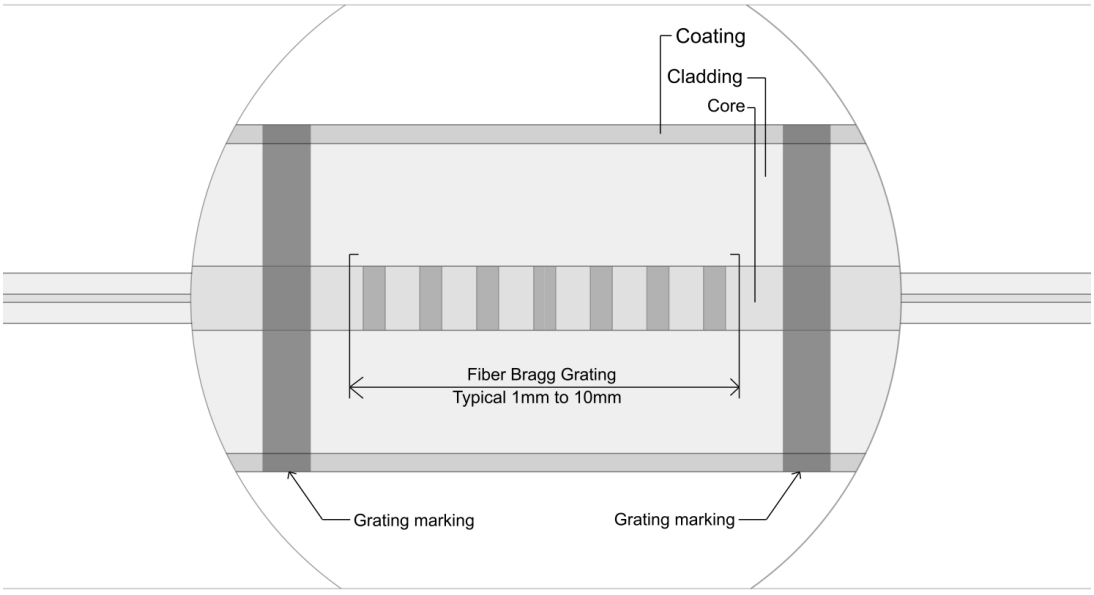

Figure 1 Periodic structure of FBG.

In order to deal with metal corrosion, the world losses almost 1000 billion dollars every year. Metal corrosion is a chemical natural process, converting metal to a chemically stable form, usually its hydroxide or sulfide. This process is very slow, usually costing weeks or months to cause an obvious change in structure without human interference. Under most conditions, the change caused by corrosion is considered as damage to structure, usually dangerous. However, at different time, different actions are needed to handle corrosion. We need a way to monitoring corrosion process, in order to determine what kind of action we need. Several physical properties of the structure will change during corrosion in regular way [13]. Corrosion Monitoring can be realized through finding the regularity and measuring these properties by signals connected to them, such as the strain of the structure, the temperature, the PH value around the corrosion area and so on [13]. However, well-developed monitoring corrosion systems are not cheap or with low accuracy. The detection part of monitoring system will be placed in the corrosion environment, where the corrosion can also happen on. In order to handle this, the most commonly solution is putting the detection part needs in sealed package, always in big size, resulting in non-negligible damage to the detected structure [14], [15]. Several detection parts' designs are very small and the related influence on the structure can be negligible, however, this kind of detective parts always need to be replaced frequently, very expensive [16].

Recent years, corrosion monitoring systems based on FBG sensors have been emphasized and rapidly developed [16]–[18]. FBGs based corrosion monitoring systems have many advantages over others. First, the detection part of this system is optic fiber, which is made by quartz, very stable and very cheap. Also, different coatings can be applied on the fiber, making it even better. Second, this system is very small. The only part needs to put into the structure is several meters long fiber, as thick as human hair. The change caused by the embedding can be

ignored without any problem. Third, this system has a long lifespan. The fiber remains the same for decades, even longer than most construction lifespan. Also, the signal used here is light, which is stable in any condition. As long as this system is set up, we can monitor the corrosion without any later adjustments under the designed environments.

1.1 History

In 1978, the group in the Canadian Research Center found the photosensitivity of optic fiber when testing Germanic-doped silica fiber [19]. This fiber reflected 4% of the incident light due to the periodic refractive index grating they written into the core of the optical fiber. These periodic gratings are called Bragg gratings, because the basic theory used here is Bragg's law. The behavior of light in the FBGs is similar to Bragg diffraction. The fundamentals of Bragg's law were promoted by Sir William L. Bragg to explain the X-ray diffraction happens in the crystal structure of thin films. In 1989, a breakthrough technique in writing gratings using external radiation was promoted by Gerry Meltz er al. [20]. They used two interfering beams with a 244nm wavelength external to fiber. With this technique, the period of the gratings, in other word, the distance between gratings, can be designed by changing the angle between the two beams, derived by

$$\lambda_B = \frac{n_{eff}\lambda_{uv}}{n_{uv}\sin\left(\frac{\theta}{2}\right)} \tag{1.1}$$

, where λ_B is the Bragg reflection wavelength, n_{eff} is the effective refractive index of the fiber, n_{uv} is refractive index of silica in UV, λ_{uv} is the wavelength of UV, θ is the angle between two incident interferometer beams. Nowadays, it is possible to write a Bragg grating in any bans, such as C-band, ranging from 1530 nm to 1565 nm.

Though the writing flexibility promoted by Meltz boosted the wave of FBGs research and application, however, it was still very difficult to fabricate a perfect interference pattern. They used an interferometer in their experiment, shown in Figure 2(a). This method requires the beams having considerably long paths in open air, resulting in a poor coherence laser due to the disturbance. As a result, a new optical part was created to overcome this problem during 1990s, called phase mask. As shown in Figure 2(b), Phase mask is a diffractive optical element, with grooves etched into silica mask plate, obtaining an interference pattern as the diffracted beams cross each other. Phase mask make the fabrication process much more efficient, which is still in use today.

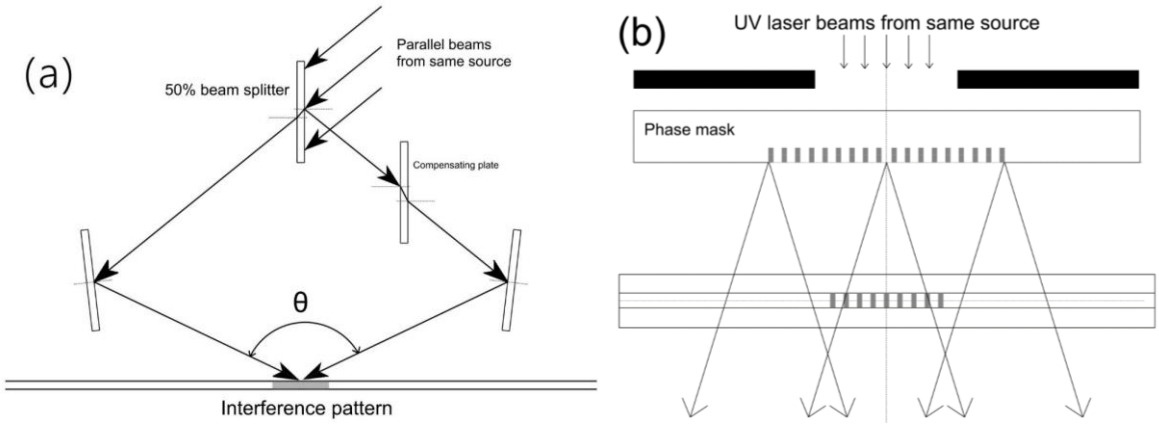

Figure 2 (a) UV interferometer for writing Bragg gratings in optic fiber; (b) Simple schematic of phase-mask geometry for inscribing Bragg gratings in optical fibres.

1.2 Background

1.2.1 Optic Fiber Sensor (OFS)

Optic fiber sensor (OFS), as its name implies, uses optic fiber as a sensor to measure some physical quantities, such as temperature, strain, humidity, voltage and so on [8], [9], [21]. OFS can allow light to travel from one end to another end of this fiber. OFS has a core and cladding layer, all mainly made by Silica (SiO_2), doped with Ge (mix Ge with SiO_2 in gaseous phase). The only difference between core and cladding is their Ge-doped percentage, which leads to the difference of refraction index (ratio of light traveling speed in certain material of the speed in vacuum) in these two parts. With proper values for the Ge-doped percentages in core and cladding, the light can be totally reflected within the core without leaking.

1.2.1.1 Intensity-based Sensors and Spectral-Based Sensors

Based on the data analysis method, OFSs are generally categorized into two classes: intensity-based sensors and spectral-based sensors. Intensity-based fiber optic sensors always has some manufacture structure that directly bring in the influence of surrounding medium, which can affect the propagation of light, resulting in the intensity change [22]–[26]. Spectral-based fiber optic sensors always have kinds of etched gratings in their fiber cores, which are very sensitive to surrounding changes, resulting in spectrum change, usually peak wavelength shift [27]–[32].

1.2.1.2 Single-mode Fiber (SMF) and Multi-mode Fiber (MMF)

Based on the ratio of the diameter of the core and the cladding layer, OFS can be divided into two main types, single-mode fiber (SMF) and multi-mode fiber (MMF), as shown in Figure 3. The core for SMF (9μm in diameter) is too small comparing to its cladding (126μm in diameter), only allowing one beam of light. Although light reflects within the core when traveling, the reflection angle is too small so that the direction of light traveling is assumed to along the fiber. For this reason, SMF has a good ability in accuracy and sensitivity. A very small change on the fiber, where the FBG is fabricated, will affect a certain range of the light signal, showing the high sensitivity. MMF can carry many beams of light for its large core. Beams different incident angle won't interfere each other, allowing a higher "light-gathering" capacity. However, due to the nonnegligible reflected angles, MMF has a lower sensitivity compared to SMF. As a result, SMF is usually used for measurement while MMF is usually used for data communication.

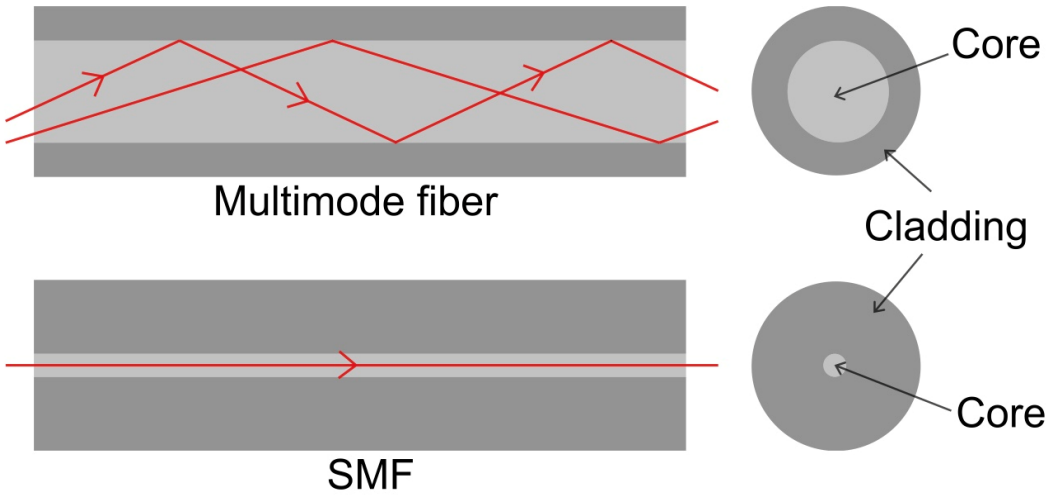

Figure 3 Structure of multi-mode fiber and single mode fiber.

1.2.2 Fiber Bragg Grating (FBG)

Fiber Bragg grating is kinds of Bragg reflectors distributed in sort of regular arrangement in an optical fiber, reflecting a certain narrow spectral band of light centered on certain wavelength, called Bragg wavelength. According to the arrangement modes of Bragg grating, FBG can be divided into uniform fiber Bragg grating, long period grating, chirped fiber Bragg grating and tilted fiber Bragg grating.

1.2.2.1 Uniform Bragg Grating and Long Period Grating

As shown in Figure 1 before, it is a uniform Bragg grating. As mentioned before, it can reflect a narrow spectral band centered on the Bragg wavelength (the peak value), as shown in Figure 4. The Bragg wavelength is sensitive to temperature and strain along the fiber, governed by Bragg grating equation [1], [33].

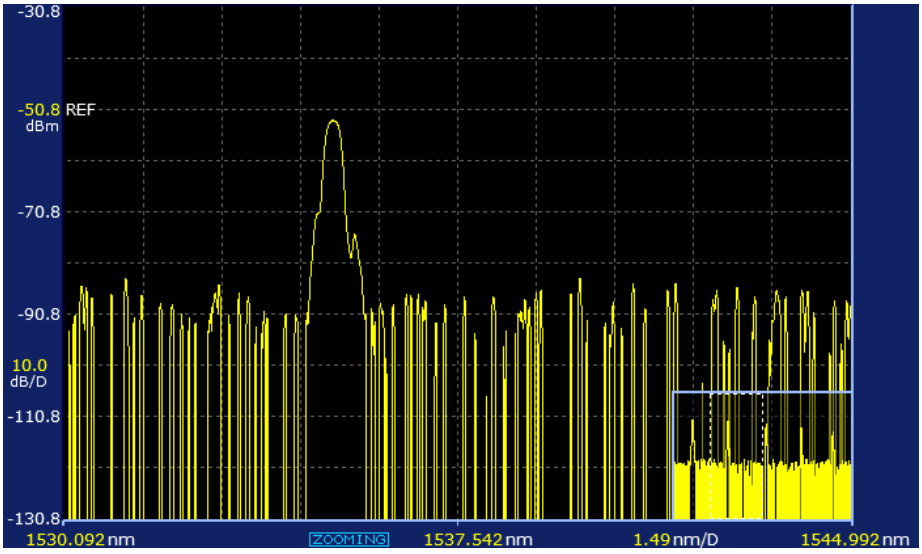

Figure 4 Reflected amplitude spectra of an FBG with Bragg wavelength at 1535.18nm, measured by AQ6374.

Long period grating (LPG) is very similar to uniform fiber Bragg grating. Their gratings are all perpendicular to the axis of the fiber. The only difference is that long period grating has a much longer distance between gratings, resulting in high sensitivity to the change of the refractive index of surrounding medium [34]. They are also sensitive to bending [31]. Different from uniform FBG, LPG has more information in the transmitted amplitude spectrum, as shown in Figure 5(b). The so called core mode and cladding modes are coupled together to build the theory [35].

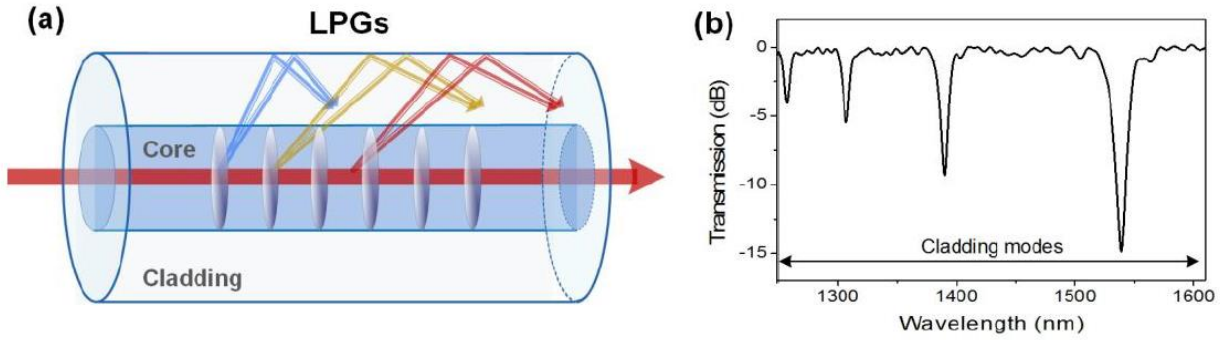

Figure 5 (a) Sketch of light mode coupling in long period grating [36]; (b) Transmitted amplitude spectrum of a 1cm-long LPG [36].

1.2.2.2 Tilted Fiber Bragg Grating (TFBG)

Tilted fiber Bragg grating (TFBG) are short period gratings (differing from LPG) with a small angle, usually small than 45 degrees, respect to the perpendicular to the axis of the fiber [37], as shown in Figure 6 (a). Similarly, TFBG also has more information in the transmitted amplitude spectrum. Figure 6(b) shows the transmission spectra for measured TFBG as a function of tilt angle [38]. By calculating the normalized area formed by the curves of the transmission spectra, the refractive index of surrounding medium can be gained [39].

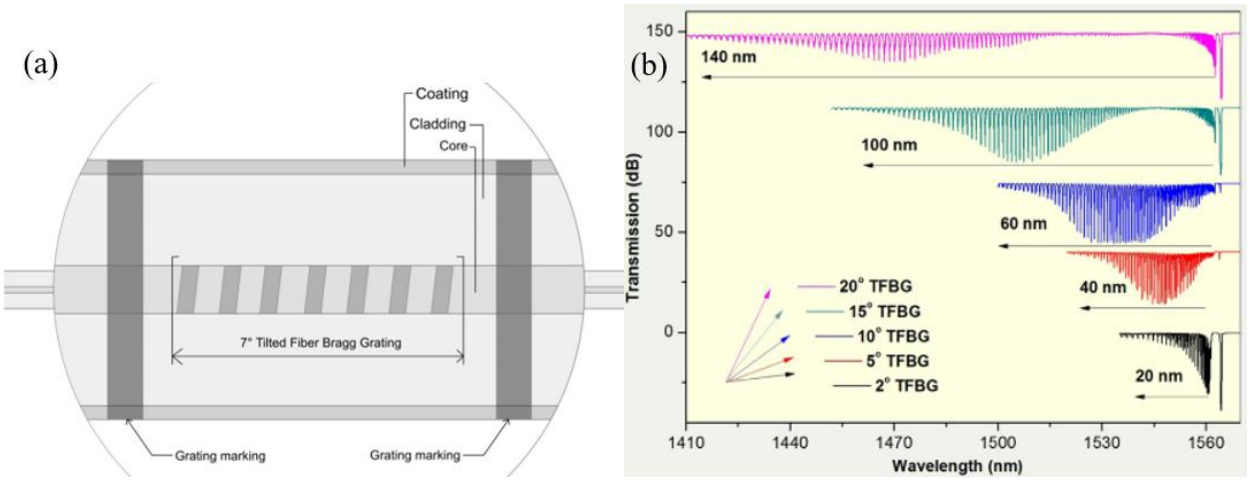

Figure 6(a) Structure of a 4 degree tilted fiber Bragg grating in SMF; (b) Measured TFBG transmission spectra as a function of tilt angle [38].

1.2.2.3 Chirped Fiber Bragg Grating (CFBG)

The grating period or the core effective refractive index of a chirped FBG vary axially as shown in Figure 7. Bragg wavelength of a CFBG is different depending on its position, resulting in a broad reflection spectrum, as shown in Figure 8. Kersey proposed the theory to describe the relationship between the broad reflection spectrum and position along the grating [40].

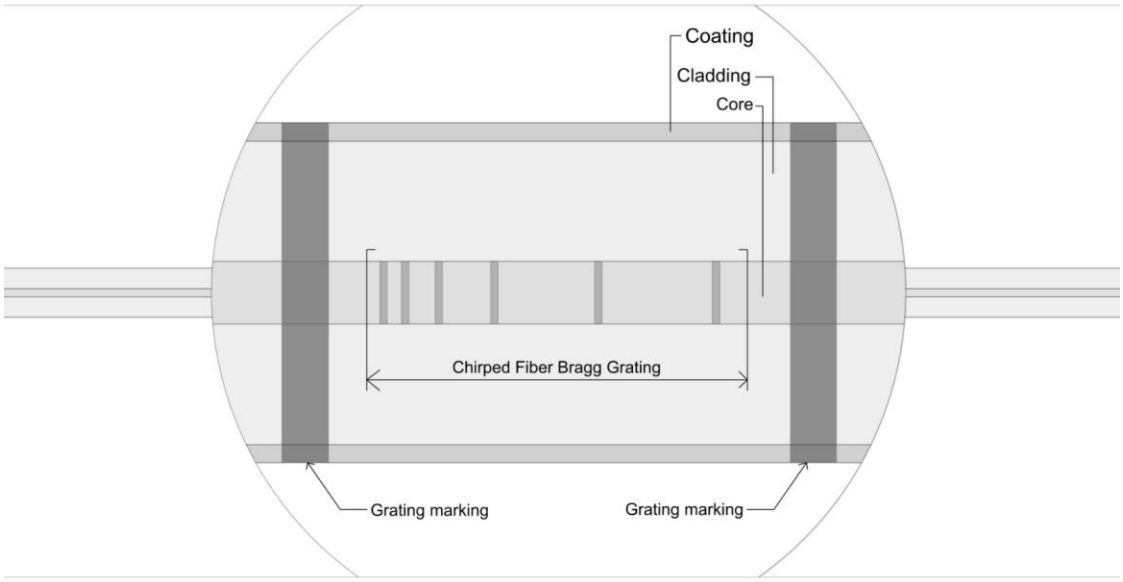

Figure 7 Structure of chirped fiber Bragg grating.

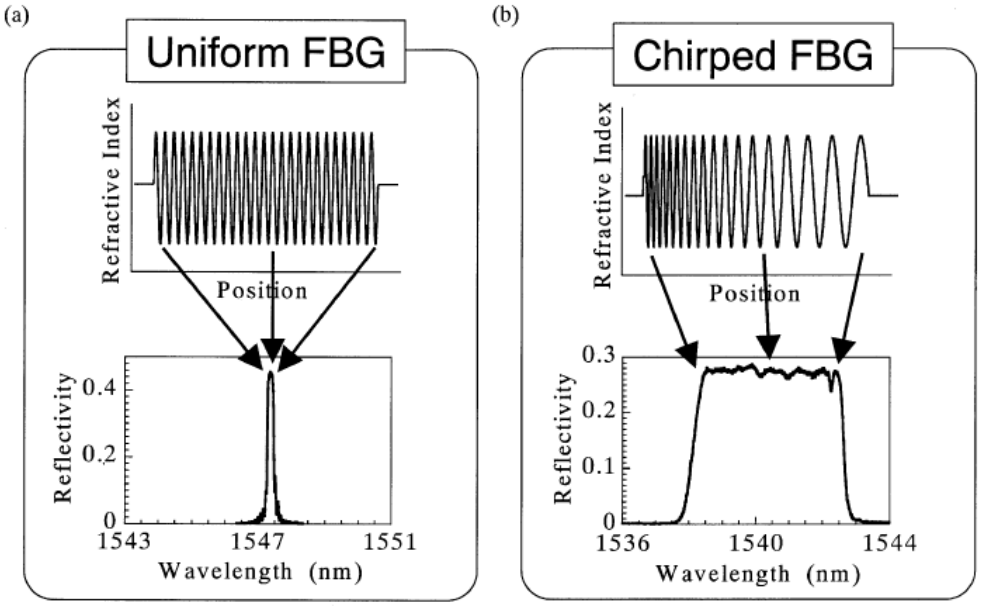

Figure 8 Profiles of refractive index and reflection spectra: (a) uniform FBG, (b) chirped FBG [41].

1.3 Basic Optical Principle

Light has wave-particle duality, meaning that it can be described in terms not only of particles, but also of waves. In physical refraction, light is treated as electromagnetic radiation, based on Maxwell equations, which has electromagnetic field, propagating through space and carrying electromagnetic radiant energy. Light can be described by three physical properties, speed **v**, wavelength $\boldsymbol{\lambda}$ and frequency **f**, with followed relationship $\boldsymbol{\lambda = \frac{v}{f}}$. Light can be divided into many bands, shown in Figure 9. Visible light, with wavelength ranging from 380nm to 740nm, between the infrared and the ultraviolet (UV). Speed of light is only determined by the propagation substance, with relationship $\boldsymbol{v = \frac{1}{\sqrt{\varepsilon\mu}}}$. According to Einstein's theory of relativity, the speed of light is constant in certain propagation substance. For example, the speed of light in a vacuum (abbreviated **c**) is exactly 299,792,458 m/s, regardless where and when the observer is.

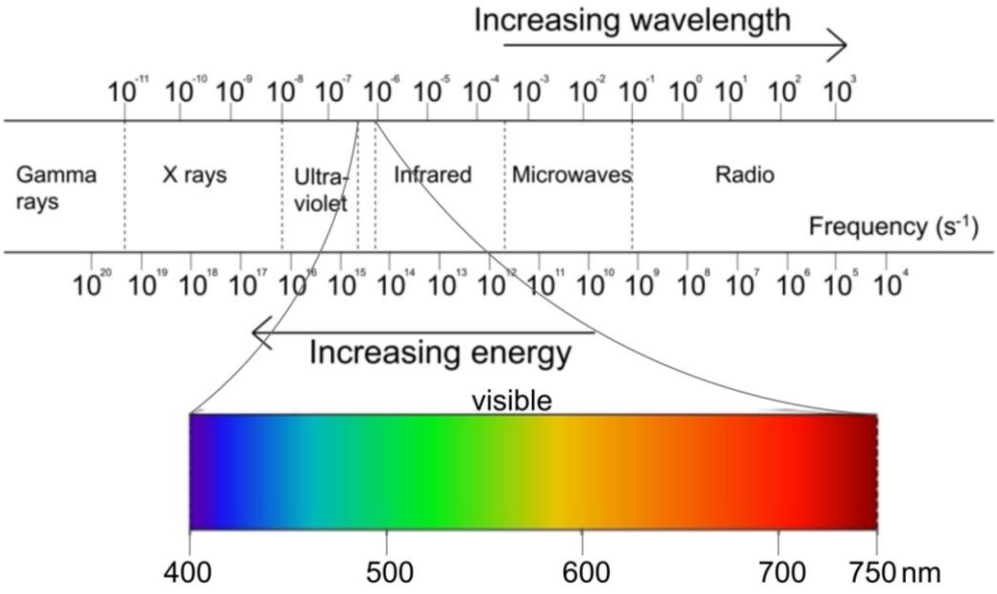

Figure 9 Electromagnetic Spectrum.

1.3.1 Reflection and Refraction of Light

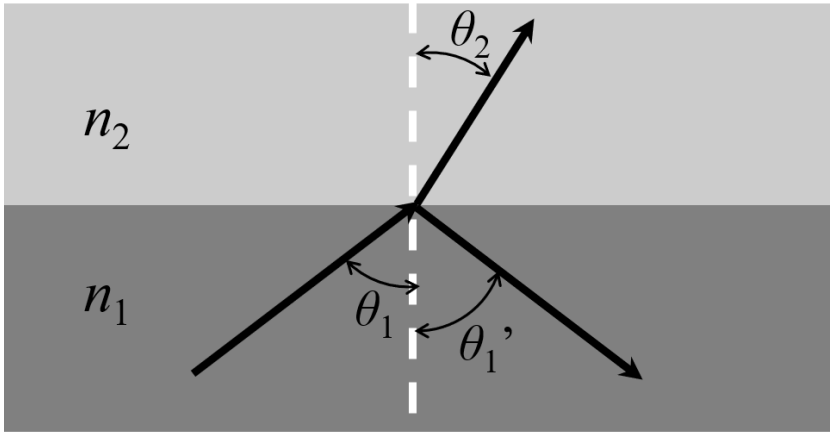

Figure 10 Reflection and Refraction of light at the interface between two media.

When light passes from one medium to another, part of the beam will change the propagating direction at the interface between two mediums, while left part will return to former medium. The reflection is simple, with relationship $\boldsymbol{\theta_1 = \theta_1'}$**.** The symbol **n** shown in Figure 10 is named refractive index, measuring how much a material refracts light. It is the ratio of the speed of the of light in a vacuum (abbreviated **c**) of the speed of light in a material (abbreviated **v**), defined as

$$\mathbf{n} = \frac{\boldsymbol{c}}{\boldsymbol{v}} \tag{1.2}$$

In 1621, Willebrord Snell derived Snell's law, explaining the relationship between the angles formed by incident light, reflected light and refracted light, when light travels from one medium to another, defined as

$$n_1 sin\theta_1 = n_2 sin\theta_2 \tag{1.3}$$

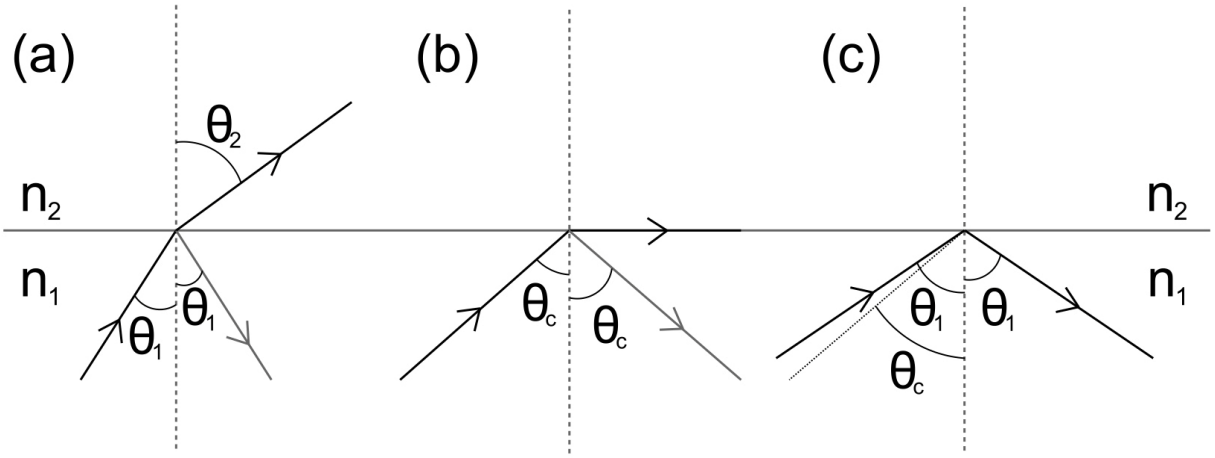

Figure 11 (a) Light passes from a denser medium to rarer medium, here n_2>n_1; (b) Critical reflection situation, θ_C is critical angle; (c) Total internal reflection situation.

When light travels from denser medium (large **n**) to rarer medium (small **n**), incident angle ($\boldsymbol{\theta_1}$) is always smaller than refraction angle ($\boldsymbol{\theta_2}$), as shown in Figure 11. Increasing $\boldsymbol{\theta_1}$ to a certain value, $\boldsymbol{\theta_C}$, the refracted light will suddenly disappear, when $\boldsymbol{\theta_2}$ reaches the value of 90°. This angle is called critical angle, shown in Figure 11(b). Applying Snell's law, $\boldsymbol{\theta_C}$ is defined as

$$\theta_C = sin^{-1}\left(\frac{n_2}{n_1}\right) \tag{1.4}$$

For any $\theta_1 > \theta_C$, total internal reflection will happen. The light cannot pass through this interface and is entirely reflected. Optic fiber is the application of total internal reflection. Because of the fiber core is very thin, light always enters the fiber with a big angle, greater than θ_C, as shown in Figure 12.

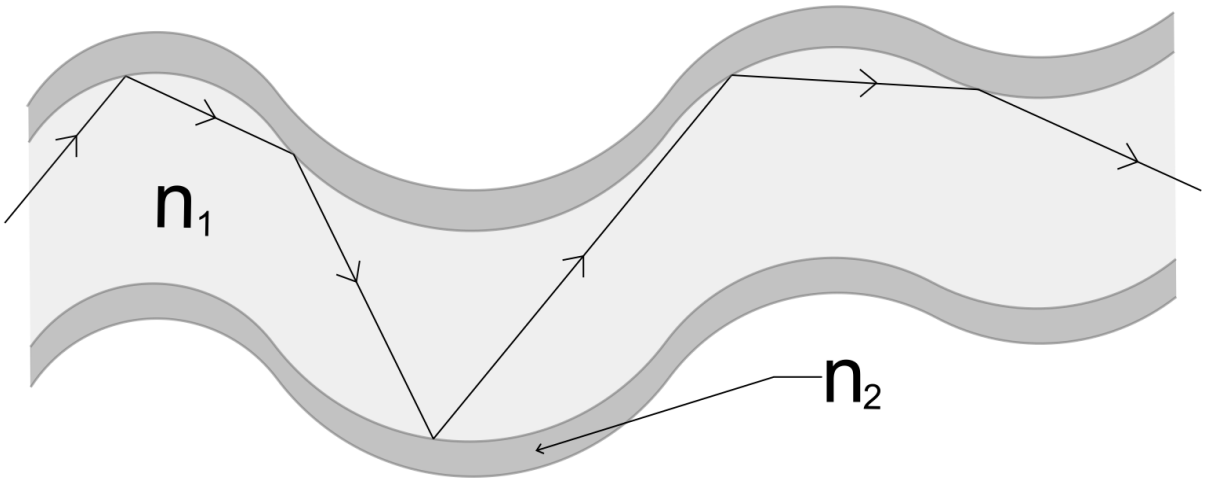

Figure 12 Path of total internal reflection light in an optic fiber.

1.3.2 Interference of Light

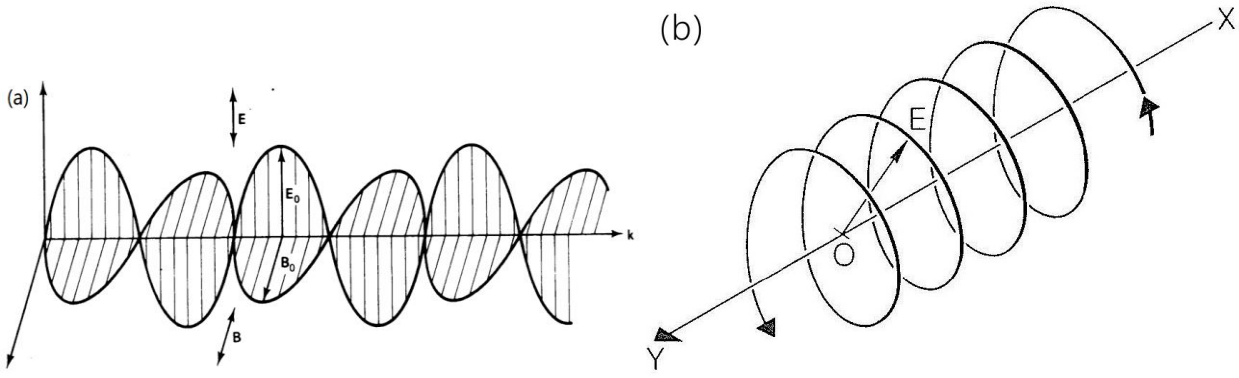

Figure 13 (a) The magnetic field (B) and electric field (E) of a circularly polarized light, perpendicular to energy transfer direction; (b) Real propagation path for a circularly polarized light in space, circularly refering the polarization direction (electric).

Light is an electromagnetic wave (transverse wave), having oscillations occurring perpendicular to the direction of energy transfer, shown in Figure 13. By convention, the polarization direction is given by its electric field vector. Maxwell equations are linear equations, resulting in the principle of superposition of waves, the electric field (E) can be linearly superimposed. The electric field, $\mathrm{E}(\mathrm{P},\mathrm{t})$, formed by N waves at point P, defined as

$$\vec{\mathrm{E}}(\mathrm{P},\mathrm{t}) = \sum_{n=1}^{N} \vec{E}_n(P,t) \tag{1.5}$$

For a monochromatic light, electric field (E) can derived in plural form

$$\vec{E}_i(P,t) = \vec{E}_0(P)e^{i[\omega t+\phi(P)]} \tag{1.6}$$

$\vec{E}_i(P,t)$ is the amplitude of light at point P; $[\omega t + \phi(P)]$ represents the phase of light at point P; $\phi(P)$ is the initial phase of light. The intensity $\mathrm{I}(\mathrm{P},\mathrm{t})$ of two light is

$$\begin{aligned} I(P) &= \frac{1}{\tau}\int_0^\tau \left|\vec{E}\right|^2 dt = \frac{1}{\tau}\int_0^\tau \vec{E}\cdot\vec{E}^* dt = \langle \vec{E}\cdot\vec{E}^*\rangle \\ &= \langle(\vec{E}_1+\vec{E}_2)\cdot(\vec{E}_1^*+\vec{E}_2^*)\rangle \\ &= \langle \vec{E}_1\cdot\vec{E}_1^*\rangle + \langle \vec{E}_2\cdot\vec{E}_2^*\rangle + \langle \vec{E}_1\cdot\vec{E}_2^*\rangle + \langle \vec{E}_2\cdot\vec{E}_1^*\rangle \\ &= I_1 + I_2 + 2\vec{E}_{10}\cdot\vec{E}_{20}\langle cos\delta\rangle \end{aligned} \tag{1.7}$$

Here δ is called phase difference, given by

$$\delta = (\omega_1-\omega_2)\mathrm{t} + \phi_1(\mathrm{P}) - \phi_2(P) \tag{1.8}$$

If the two waves' oscillation directions are not vertical to each other ($\vec{E}_{10}\cdot\vec{E}_{20} \neq 0$), with same frequency ($\omega_1 = \omega_2$) and a constant initial phase difference ($\Delta\phi = \phi_1(\mathrm{P}) - \phi_2(P)$), the intensity of the two waves is not the sum of each value. These two waves are called coherent lights and this phenomenon is interference of light. For coherent lights with same oscillation direction ($\vec{E}_{10} = \vec{E}_{20}$), the intensity forms in

$$I(P) = 2I_0 + 2I_0\langle\cos(\Delta\phi)\rangle \tag{1.9}$$

If the phase difference $\Delta\phi = 2k\pi, k \in N$, then $\langle\cos(\Delta\phi)\rangle = 1$, $I(P) = 4I_0$, it is called constructive interference; if $\Delta\phi = (2k+1)\pi, k \in N$, then $\langle\cos(\Delta\phi)\rangle = 0$, $I(P) = 0$, it is the destructive interference.

1.3.3 Bragg Diffraction

Bragg diffraction (X-ray diffraction) was first discovered by Lawrence Bragg and William Henry Bragg in 1913 when they irradiated X-rays to crystalline solid [42]. At certain wavelengths and incident angles, they observed intense peaks of reflected radiation; at certain wavelengths and incident angles, the reflected radiation disappeared.

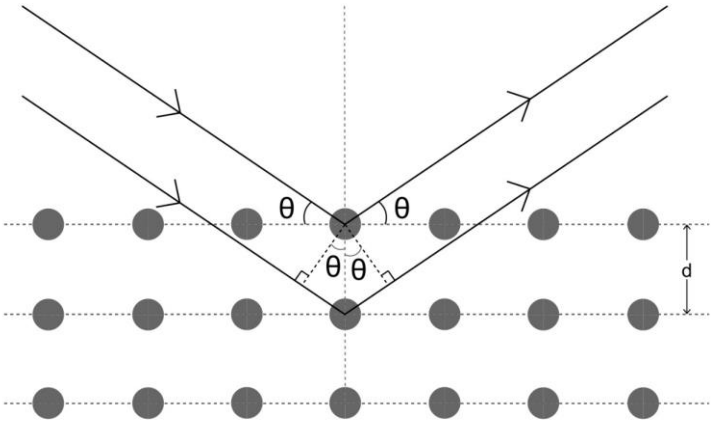

Figure 14 Bragg diffraction. Two coherent beams approach a crystalline solid and are reflected by two different atoms within it. Constructive interference occurs when lower beam traverses an extra length, equal to an integer multiple of the wavelength of the radiation.

Lawrence Bragg explained this phenomenon by modeling the crystal as many discrete parallel planes with distance $\boldsymbol{d}$, and picking two parallel beams from the X-rays shown in Figure 14 [42]. The X-rays were from same light source, with same frequency, oscillation direction and initial phase. The two beams were reflected by the atoms of the crystalline system, and lower beam travers an extra length of $2\mathrm{d}\sin\theta$. When this extra length equals to an integer multiple of the wavelength ($n\lambda$) , the phase difference is $\Delta\phi = 2\mathrm{k}\pi, \mathrm{k} \in \mathrm{N}$, constructive interference, corresponding intense peaks of reflected radiation; when it equals to integer multiple plus half of the wavelength ($\frac{k+1}{2}\lambda$), the phase difference is $\Delta\phi = (2\mathrm{k}+1)\pi, \mathrm{k} \in \mathrm{N}$, destructive interference, corresponding reflected radiation disappeared situation. This leads to Bragg's law, which describes the condition on θ for the constructive interference at intense peaks [42]:

$$2dsin\theta = n\lambda \tag{1.10}$$

, where θ is the x-ray incident angle, n is an integer, λ is the radiation wavelength.

1.4 Germanium-Doped Silica Fiber

The most widely used SMF standard is SMF28, which has $8.2\mu\mathrm{m}$ core diameter, $125\mu\mathrm{m}$ cladding diameter and $245\mu\mathrm{m}$ coating diameter, optimized for use in the $1310\mathrm{nm}$ wavelength region and $1550\mathrm{nm}$ wavelength region. Germanium is one of the most common core dopants, belongs to Group IVA, same as silicon. SMF 28 is a Germanium-doped silica fiber, produced by combing gaseous Germania and silica at high temperature, undergoing a process called modified chemical vapor deposition (MCVD). In this process, Germanium can replace silicon within the

tetragonal unit cell, where coordinated with four oxygen atoms in glass, shown in Figure 15, forming in Ge-related defects in the fiber. This results in the increase of the refractive index of the core where the Ge- related defects lies, meeting the requirement of total refraction.

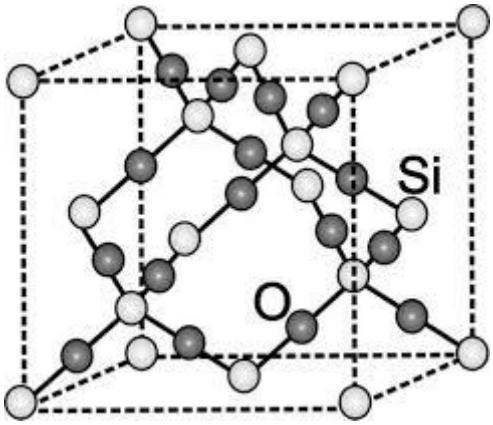

Figure 15 Unit cell of silica; blue ball represents Silicon atoms while red ball represents oxygen atoms [43].

1.4.1 Structure for Glass Fibers

Low optic loss is very important for optic fiber application, which finally achieved a value of 0.2 dB per km in recent years, achieved by the Germanium-doped fiber. The structure and refractive index distribution of an optical fiber is shown in Figure 16. The silica core has a higher refractive index than the cladding material by doping Germanium, making it possible for total internal reflection happening at the core-cladding boundaries. Typically, the difference between core and cladding refractive index for SMF working at 1550nm is around 4.5×10^{-3} with a 8μm core [33]. If add Fluorine and Boron in Germanium-doped fiber, the refractive index will decrease. With Fluorine, small index reductions (~0.1%) are possible; with Boron, large index reductions (~2%) are possible [33].

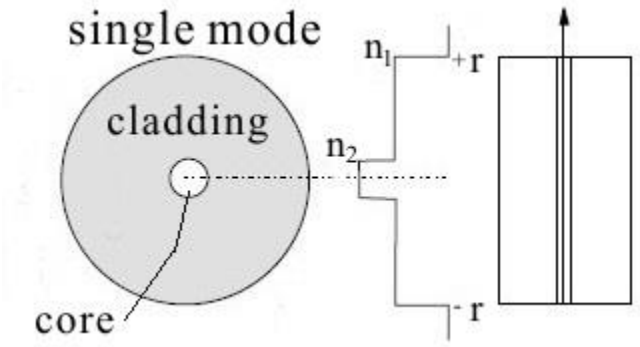

Figure 16 Cross-section of a SMF with the corresponding refractive index.

1.4.2 Refractive Index of Glass

For circular polarized light, the wavelength independence of refractive index n is given by Sellmeier expression, where λ is vacuum wavelength, and B_i and C_i are experimentally determined Sellmeier coefficients, given in Table 1 [44],

$$n^2 = 1 + \sum_{i=1}^{3} \frac{B_i \lambda^2}{\lambda^2 - C_i^2}. \tag{1.11}$$

The refractive index n, corresponding to the phase velocity v, the velocity of the phase of propagating wave. To describe the velocity of energy transmission, the group velocity v_g is defined as

$$v_g = \frac{c}{n - \lambda \frac{dn}{d\lambda}} \tag{1.12}$$

and the corresponding index N, is called group index, defined as

$$N = \frac{c}{v_g} = n - \lambda \frac{dn}{d\lambda} \tag{1.13}$$

Table 1 Values of Sellmeier coefficients for silica doped with different dopants [44].

Sample Dopant (mole percentage)	A GeO_2 (19.3)	B GeO_2 (6.3)	C GeO_2 (10.5)	D Pure SiO_2
B_1	0.005847345	0.07290464	0.05202431	0.004679148
B_2	0.01552717	0.01050294	0.01287730	0.01351206
B_3	97.93484	97.93428	97.93401	97.93400
C_1	0.7347008	0.7083952	0.7058489	0.6961663
C_2	0.4461191	0.4203993	0.4176021	0.4079426
C_3	0.8081698	0.89747794	0.8952753	0.8974794

The analytical solutions for Maxwell's equations are transversely polarized eigenmodes. The refractive index of the μth x-polarized mode, usually called effective refractive index n_{eff}, is given by [1] , where a is the diameter of the fiber core.

$$n_{eff} = n_{cladding}\left[b\left(\frac{n_{core} - n_{cladding}}{n_{cladding}}\right) + 1\right]$$

$$\begin{cases} v = \dfrac{2\pi a}{\lambda}\sqrt{n_{core}^2 - n_{cladding}^2} \\ u = \dfrac{2\pi a}{\lambda}\sqrt{n_{core}^2 - n_{eff}^2} \\ b = \dfrac{v^2 - u^2}{u^2} \end{cases} \tag{1.14}$$

1.5 Fabrication of Bragg Gratings

One of the most efficient method for writing Bragg Gratings in optic fiber is the phase mask technique. The center of this method is phase mask, which is simply to setup and reproducible. With the grooves etched into its silica plate, phase mask can diffract an incident UV beam into several orders, $m = 0, \pm 1, \pm 2 \cdots$. For uniform Bragg gratings writing (period is constant along FBG), the UV beam is at normal incidence and diffracted beam only split into $m = 0$ and $m = \pm 1$ orders, as shown in Figure 17 (a).

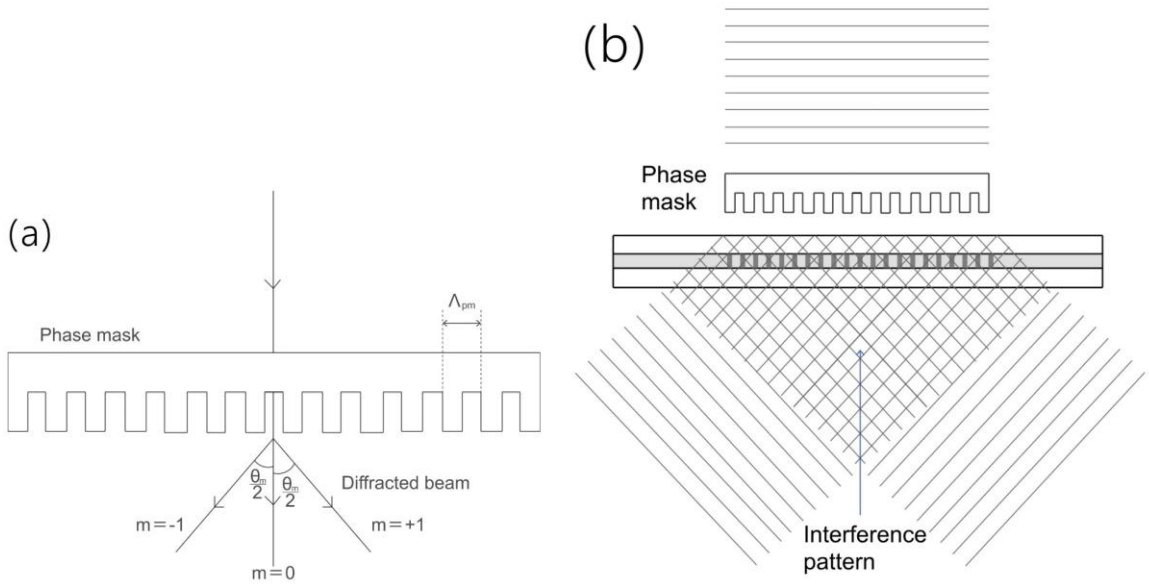

Figure 17 (a) Diffraction of a beam at normal incidence from a phase mask; (b) Fabrication of FBG using phase mask.

The interference pattern at the fiber, shown in Figure 17 (b), has a period Λ_g, related to the diffraction angle ($\frac{\theta_m}{2}$) and the period of phase mask (Λ_{pm}) by, where λ_{uv} is the UV wavelength

$$\Lambda_g = \frac{\lambda_{uv}}{2sin\frac{\theta_m}{2}} = \frac{\Lambda_{pm}}{2}. \quad (1.15)$$

Bragg conditions on FBG are,

$$N\lambda_{Bragg} = 2n_{eff}\Lambda_g \quad (1.16)$$

, where $N \geq 1$ is an integer indicating the order of grating period, for uniform gratings writing $N = 1$. Then the relationship between Λ_m and λ_{Bragg} is built as

$$N\lambda_{Bragg} = n_{eff}\Lambda_{pm} \quad (1.17)$$

The period Λ_{pm} of the gratings etched in phase mask can be pre-calculated and determined by the Bragg wavelength λ_{Bragg} of FBG in the fiber.

2.0 Theoretical Analysis

2.1 Principles of Optical Fiber Bragg Grating Sensors

Bragg conditions on uniform FBG are,

$$\lambda_{Bragg} = 2n_{eff}\Lambda \tag{2.1}$$

, where λ_{Bragg} is the Bragg wavelength, Λ is the period of gratings and n_{eff} is the effective refractive index.

Assuming Y is an external parameter to be sensed by FBG, such as temperature, strain, pressure, voltage, or refractive index of a fluid. The dependence of the Bragg wavelength on these parameters can be promoted by its total derivative,

$$\frac{d\lambda_{Bragg}}{dY} = 2\frac{d}{dY}n_{eff}\Lambda = 2\Lambda\frac{dn_{eff}}{dY} + 2n_{eff}\frac{d\Lambda}{dY} \tag{2.2}$$

While the thermal expansion coefficient α is defined as,

$$\alpha = \frac{1}{\Lambda}\frac{d\Lambda}{dT} \tag{2.3}$$

similarly, we define β, the coefficient of physical length changes dependent on this external parameter, as,

$$\beta = \frac{1}{\Lambda}\frac{d\Lambda}{dY} \tag{2.4}$$

Then, we can get

$$\frac{1}{\lambda_{Bragg}}\frac{d\lambda_{Bragg}}{dY} = \frac{2\Lambda}{\lambda_{Bragg}}\frac{dn_{eff}}{dY} + \frac{2n_{eff}\Lambda}{\lambda_{Bragg}}\beta \tag{2.5}$$

Substituting Bragg conditions

$$\frac{1}{\lambda_{Bragg}}\frac{d\lambda_{Bragg}}{dY} = \frac{2\Lambda}{2n_{eff}\Lambda}\frac{dn_{eff}}{dY} + \frac{2n_{eff}\Lambda}{2n_{eff}\Lambda}\beta$$

$$\frac{1}{\lambda_{Bragg}}\frac{d\lambda_{Bragg}}{dY} = \frac{1}{n_{eff}}\frac{dn_{eff}}{dY} + \beta$$

$$\frac{d\lambda_{Bragg}}{\lambda_{Bragg}} = \frac{1}{n_{eff}}\frac{dn_{eff}}{dY}dY + \beta dY \tag{2.6}$$

, where the term $\frac{1}{n_{eff}}\frac{dn_{eff}}{dY}$ is coefficient of effective index changes of this mode dependent on this external parameter. So, this external parameter changes the physical length and the effective index of the FBG, resulting the change in Bragg wavelength. $\frac{1}{n_{eff}}\frac{dn_{eff}}{dY}$ and β are experimentally determined parameters. Then with the wavelength change, we can calculator the change of this external parameter.

2.1.1 Temperature Measurement

For the temperature measurement, external parameter Y is temperature T. So, we have,

$$\frac{d\lambda_{Bragg}}{\lambda_{Bragg}} = \frac{1}{n_{eff}}\frac{dn_{eff}}{dT}dT + \alpha dT \tag{2.7}$$

α is the thermal expansion coefficient, defined in equation (2.3),

Another term, $\frac{1}{n_{eff}}\frac{dn_{eff}}{dT}$ is defined as the thermal-optic coefficient of fiber, as η. This is the ratio of the variation of the refractive index of the fiber of the temperature change. Then, we have

$$\frac{d\lambda_{Bragg}}{\lambda_{Bragg}} = \eta dT + \alpha dT = (\alpha + \eta)dT \tag{2.8}$$

2.1.2 Strain Measurement

For the strain measurement, external parameter Y is displacement L. So, we have,

$$\frac{d\lambda_{Bragg}}{\lambda_{Bragg}} = \frac{1}{n_{eff}}\frac{dn_{eff}}{d\mathrm{L}}d\mathrm{L} + \frac{1}{\Lambda}\frac{d\Lambda}{dL}dL \tag{2.9}$$

Dividing both side with L_{FBG}, usually 1mm to 10mm, the length of FBG along propagating direction,

$$\frac{d\lambda_{Bragg}}{L_{FBG}\lambda_{Bragg}} = \frac{1}{n_{eff}}\frac{dn_{eff}}{d\mathrm{L}}\frac{d\mathrm{L}}{L_{FBG}} + \frac{1}{\Lambda}\frac{d\Lambda}{dL}\frac{d\mathrm{L}}{L_{FBG}} \tag{2.10}$$

, while the strain is defined as

$$\frac{dL}{L_{FBG}} = \varepsilon_{FBG} \tag{2.11}$$

Substituting back

$$\frac{d\lambda_{Bragg}}{\lambda_{Bragg}} = \frac{L_{FBG}}{n_{eff}}\frac{dn_{eff}}{d\mathrm{L}}\varepsilon_{FBG} + \frac{L_{FBG}}{\Lambda}\frac{d\Lambda}{dL}\varepsilon_{FBG} \tag{2.12}$$

Rearranged,

$$\frac{d\lambda_{Bragg}}{\lambda_{Bragg}} = \frac{\frac{dn_{eff}}{n_{eff}}}{\frac{d\mathrm{L}}{L_{FBG}}}\varepsilon_{FBG} + \frac{\frac{d\Lambda}{\Lambda}}{\frac{dL}{L_{FBG}}}\varepsilon_{FBG} \tag{2.13}$$

, where $\frac{d\Lambda}{\Lambda}$ is the strain change of grating period and $\frac{dL}{L_{FBG}}$ is the strain change of FBG. The grating period and FBG are in the same fiber, always undergoing same strain change, so

$$\frac{\frac{d\Lambda}{\Lambda}}{\frac{dL}{L_{FBG}}} = 1 \tag{2.14}$$

Another term, $\frac{\frac{dn_{eff}}{n_{eff}}}{\frac{dL}{L_{FBG}}}$ is defined as the photo-elastic coefficient of fiber, as ρ_e. This is the ratio of the variation of the refractive index of the fiber of the applied strain, usually negative. Then, we have

$$\frac{d\lambda_{Bragg}}{\lambda_{Bragg}} = \rho_e \varepsilon_{FBG} + \varepsilon_{FBG} = (1 + \rho_e)\varepsilon_{FBG} \tag{2.15}$$

2.1.3 Classical Bragg Grating Equation

Usually, temperature measurement and strain measurement always interact with each other. So, combing equation for temperature and strain produces the sensitivity of the Bragg wavelength, the classic Bragg grating equation,

$$\frac{\Delta\lambda_{Bragg}}{\lambda_{Bragg}} = (1 + \rho_e)\varepsilon_{FBG} + (\alpha + \eta)\Delta T \tag{2.16}$$

, where ε_{FBG} is the strain change along the fiber axial direction and ΔT is the temperature change in adjacent areas around FBG. The parameter in this equation for a silica fiber with a Germanium-doped core are $\rho_e = -0.22$, $\alpha = 0.55 \times 10^{-6}/℃$ and $\eta = 8.6 \times 10^{-6}/℃$ [1].

For a typical FBG with Bragg wavelength at 1550nm, after substituting these values, the sensitivity of the FBG to temperature and strain are

$$\begin{aligned} \frac{\Delta\lambda_{Bragg}}{\lambda_{Bragg}} &= 14.18\ pm/℃ \\ \frac{\Delta\lambda_{Bragg}}{\lambda_{Bragg}} &= 1.2\ pm/\mu\varepsilon \end{aligned} \tag{2.17}$$

2.2 Average Strain Transfer Rate for the Single Face Bonded FBG

The basic structure of a single face bonded FBG is shown in Figure 18. r_f is the radius of the fiber core and cladding layer, usually 63μm. r_c is the radius of the polyimide coating, 78μm. r_a is the radius of the adhesive layer bonded with the host material. The bond length is 2L.

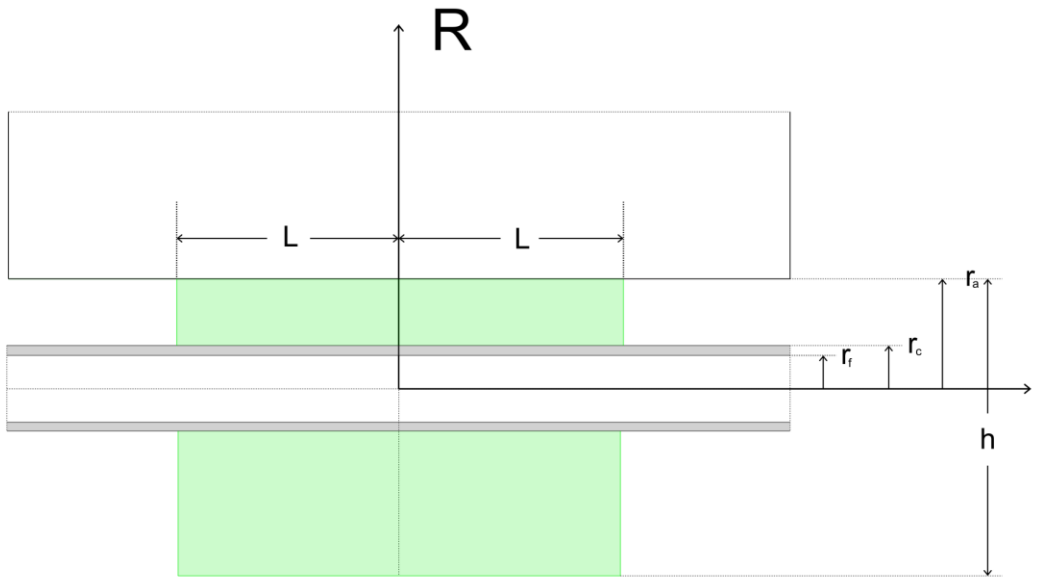

Figure 18 Structure of a single face bonded FBG.

Assume the host material is uniformly strained, and the core and cladding of the SMF are same, and there are no strain discontinuities across any interface. Assume the strains at ends of adhesive layer are zero, $\varepsilon_f(-L) = \varepsilon_f(L) = 0$. The relationship between the strain on the SMF and the strain on the outer fiber of the adhesive layer along the SMF is [45]

$$\frac{d^2\varepsilon_f(x)}{dx^2} - \alpha^2\varepsilon_f(x) = -\alpha^2\varepsilon_a(x)$$
$$\varepsilon_f(x) = \varepsilon_a(x)[1 - \frac{\cosh(\alpha x)}{\cosh(\alpha L)}] \quad (2.18)$$

$$\alpha = \left\{\frac{r_f^2\left(E_f - E_c\right)\ln\left(\frac{r_c}{r_f}\right)}{2G_c} + \frac{\pi r_a\left[r_f^2 E_f + \left(r_c^2 - r_f^2\right)E_c\right]}{2r_c G_a} + (1+\mu_a)[h^2 - (h - r_a - r_c)^2] + \frac{1}{2}(1+\mu_c)(r_c^2 - r_f^2)\right\}^{-\frac{1}{2}}$$

, where α represents the numerical relation between the strain in FBG and adhesive, given by [45]. After considering the anti-plane stress applied on the measured surface, with the true strain on the host material ε_m, strain on the adhesive layer can be expressed as [45]

$$\varepsilon_a(x) = \beta\varepsilon_m \tag{2.19}$$

The factor β is defined to express the reinforcement effect on the host material, determined by [45]

$$\beta = 1 + \frac{2\alpha EA(1+\mu_m)}{\pi E_m \cosh(\varepsilon_m \alpha L)}\int_0^L \frac{\sinh(\alpha x)\left[(\mu_m - 1)w^2 - 4x^2\right]}{x(4x^2 + w^2)^{1.5}}dx \tag{2.20}$$

Regard the average of the strain along the FBG, within length L_f, as the equivalent strain sensed by FBG [45]

$$\varepsilon_{FBG} = \frac{2\int_0^{\frac{L_f}{2}} \varepsilon_f(x)dx}{L_f} = \beta\varepsilon_m\left[1 - \frac{2\sinh\left(\frac{\alpha L_f}{2}\right)}{\alpha L_f \cosh(\alpha L)}\right] \tag{2.21}$$

$$k = \frac{\varepsilon_m}{\varepsilon_{FBG}} = \beta\left[1 - \frac{2\sinh\left(\frac{\alpha L_f}{2}\right)}{\alpha L_f \cosh(\alpha L)}\right] \tag{2.22}$$

The average strain rate k for the $250\mu m$ (in diameter) acrylate coating FBG with different adhesive length is shown in Table 2.

Table 2 Average strain rate k attained by experiment [45], the thickness of adhesive layers are all $\mathbf{2 \times 0.65}$ (mm).

$2L_f\ (mm)$	$2L\ (mm)$	W (mm)	k_e	k_t
10	16.01	3.01	1.3966	1.4368
10	20.02	2.85	1.2519	1.2350
10	23.23	3.15	1.1543	1.1494
10	27.35	3.24	1.0978	1.0864
10	31.40	3.09	1.0592	1.0514

Therefore, an adequate length of SMF must be bonded to make the average strain rate is close to one. The reasonable adhesive length $(2L)$ is expected to be larger than $8L_f$.

2.3 Four-point Bending Model

2.3.1 Beam Bending Strain

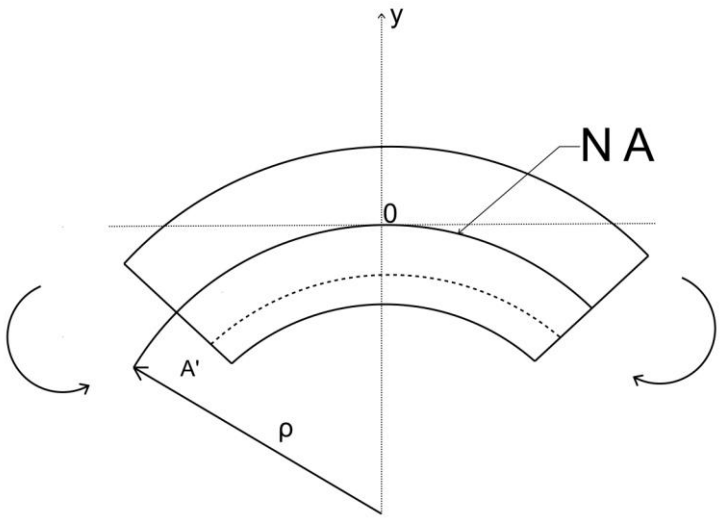

Figure 19 Analysis for small beam element under bending.

Figure 19 shows the basic strain model for a bending beam. Assume y, the distance upward from neutral axis (NA), is small enough to treat the radius of curvature of this element is a constant value, ρ. So, the normal strain at line A'B' is, also called engineering strain,

$$\varepsilon = \frac{\overline{A'B'} - \overline{NA}}{\overline{NA}} = \frac{(\rho + y)d\theta - \rho d\theta}{\rho d\theta} = \frac{y}{\rho} \tag{2.23a}$$

So, the strain is only related with the distance from the NA, if NA is fixed.

Logarithmic strain is defined as,

$$\mathrm{d}\varepsilon_{log-x} = \frac{dx}{x} \tag{2.23b}$$

After integral, relationship between engineering strain and logarithmic strain is,

$$\varepsilon_{log-x_i} = ln\left(1 + \frac{\Delta L_i}{L_i}\right) = ln(1 + \varepsilon_{x_i}) \tag{2.23c}$$

2.3.2 Poisson's ratio influence on the cross section

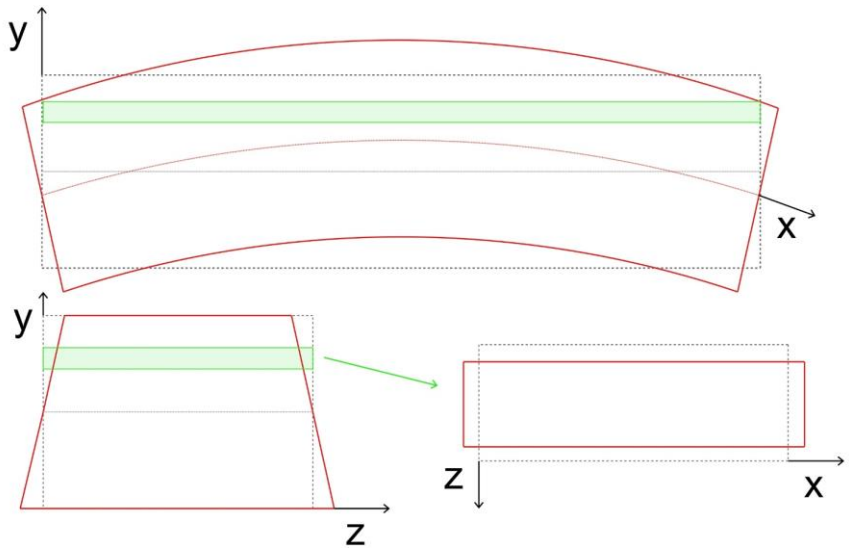

Figure 20 Illustration of bending influence on cross section.

For isotropic materials, Poisson's ratio ν is same in all direction. Assume the strain of carbon steel plate only happens in x and z direction. The expected changes of form are shown in Figure 20. The radiuses of curvature of elements are treated the same. The x-axis is the neutral axis. The definition of the Poisson's ratio is, ($d\varepsilon_{log}$ is the logarithmic strain, while ε is engineering strain),

$$\nu = -\frac{d\varepsilon_{log-z}}{d\varepsilon_{log-x}}, \qquad \nu = -\frac{d\varepsilon_{log-y}}{d\varepsilon_{log-x}}, \qquad d\varepsilon_{log-x_i} = \frac{dx_i}{x_i} \tag{2.24}$$

So, for an element marked as green area, assume the changes in x y and z are ΔL Δdy and $\Delta W, \gamma_{xz} = \gamma_{zx} = 0$

$$-\nu\int_{L}^{L+\Delta L}\frac{dx}{x}=\int_{W}^{W+\Delta W}\frac{dz}{z}=\int_{dy}^{dy+\Delta dy}\frac{dy}{y}$$
$$(1+\frac{\Delta L}{L})^{-\nu}=1+\frac{\Delta W}{W}=1+\frac{\Delta \mathrm{dy}}{dy} \tag{2.25}$$

Applying first order estimation, since $\frac{\Delta L}{L}$ is every small, so

$$1-\nu\frac{\Delta L}{L}=1+\frac{\Delta W}{W}=1+\frac{\Delta \mathrm{dy}}{dy}$$
$$-\nu\frac{\Delta L}{L}=-\nu\varepsilon_x=-\nu\frac{y}{\rho}=\frac{\Delta W}{W}=\varepsilon_z=\frac{\Delta \mathrm{dy}}{dy} \tag{2.26}$$
$$\Delta \mathrm{dy}=-\nu\frac{y}{\rho}\mathrm{dy},\qquad \Delta \mathrm{y}=\int_0^y-\nu\frac{y}{\rho}dy=-\nu\frac{y^2}{2\rho}$$
$$\Delta L=L\frac{y}{\rho},\qquad \Delta W=-\nu W\frac{y}{\rho},\qquad \Delta t_y=-\nu\frac{y^2}{2\rho}$$

In conclusion, the relationship for strains in three directions are

$$\varepsilon_z=-\nu\varepsilon_x,\qquad \varepsilon_y\big|_{at\ y}=\frac{\Delta t_y}{y}=-\nu\frac{y}{2\rho}=-\frac{\nu}{2}\varepsilon_x \tag{2.27}$$

Hooke's law for isotropic materials is written as,

$$\begin{bmatrix}\sigma_{xx}\\ \sigma_{yy}\\ \sigma_{zz}\\ \sigma_{xy}\\ \sigma_{yz}\\ \sigma_{zx}\end{bmatrix}=\frac{E}{(1+\nu)(1-2\nu)}\begin{bmatrix}1-\nu & \nu & \nu & 0 & 0 & 0\\ \nu & 1-\nu & \nu & 0 & 0 & 0\\ \nu & \nu & 1-\nu & 0 & 0 & 0\\ 0 & 0 & 0 & 1-2\nu & 0 & 0\\ 0 & 0 & 0 & 0 & 1-2\nu & 0\\ 0 & 0 & 0 & 0 & 0 & 1-2\nu\end{bmatrix}\begin{bmatrix}\varepsilon_{xx}\\ \varepsilon_{yy}\\ \varepsilon_{zz}\\ \gamma_{xy}\\ \gamma_{yz}\\ \gamma_{zx}\end{bmatrix} \tag{2.28}$$

Combined with equation (2.23) and (2.27),

$$\sigma_{xx}=\frac{1-\nu-\frac{3}{2}\nu^2}{1-\nu-2\nu^2}E\varepsilon_{xx}=E'\varepsilon_{xx} \tag{2.29}$$

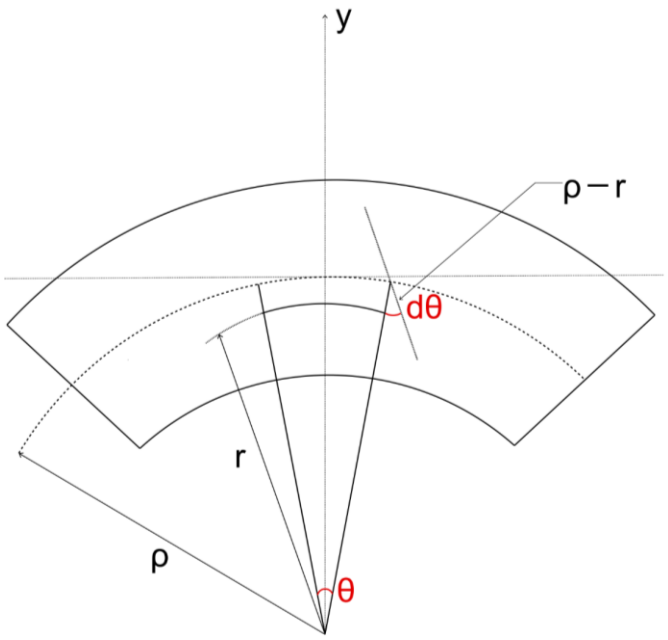

Figure 21 NA position for curved beam.

For a curved beam, assume a virtual moment is applied,

$$\delta\varepsilon = \frac{(\rho - r)d\theta}{r\theta} = \frac{d\theta}{\theta}\frac{\rho - r}{r} \tag{2.30}$$

The strain in equation (2.30) is used to describe the strain change compared to the curved beam, while equation (2.23a) is used to describe the strain change compared to straight beam.

Apply equilibrium of force in x-direction,

$$\sum F_x = 0 = \iint_A \delta\sigma dA = \iint_A E'\delta\varepsilon dA$$

$$\rho = \frac{A}{\iint \frac{dA}{\rho}} \tag{2.31}$$

For a trapezoidal cross section with upper side W_1, bottom side W_2 and height h,

$$\rho = \frac{1}{2}\frac{(W_1 + W_2)h}{W_1 - W_2 + \frac{W_2 r_o - W_1 r_i}{h} ln\frac{r_o}{r_i}} \tag{2.32}$$

For this four-point bending specimen, the parameters are $\mathrm{H} = 120\mathrm{mm}, \mathrm{A} = 27\mathrm{mm}, \Delta = 2\mathrm{mm}$. Then the radius of curvature r_i for this model is $446.72055\mathrm{mm}$. The parameters for the carbon steel plates are $\mathrm{L} = 135\mathrm{mm}, \mathrm{W} = 50\mathrm{mm}, \mathrm{t} = 1.59\mathrm{mm}$. The sensitivity of the spectrum used is $1.67 \pm 0.01\mu\varepsilon$. First assume the NA is at *h*/2 after bending. Then for upper face and bottom face of carbon steel plate,

$$\Delta \mathrm{t}_{\pm\frac{t}{2}} = -\nu\frac{y^2}{2\rho} = -\nu\frac{\left(\pm\frac{h'}{2} \pm \Delta\rho\right)^2}{2\rho} = -\nu\frac{h^2}{8\rho}\Big|_{\Delta\rho=0}$$

$$h' = \mathrm{h} + \Delta \mathrm{t}_{+\frac{h}{2}} - \Delta \mathrm{t}_{-\frac{h}{2}} = \frac{t}{1 + \frac{4\nu\Delta\rho}{2\rho}} \tag{2.33}$$

$$\Delta W_{upper} = -0.02665mm, \qquad \Delta W_{below} = 0.02665mm,$$

$$\Delta L_{upper} = 0.2398mm, \qquad \Delta L_{below} = -0.2398mm$$

Apply equation (2.32), a new ρ achieved. Then substitute back to equation (2.33). Repeat this loop until stable.

$$\rho = 447.51539\mathrm{mm}, \Delta\rho = 0.00016mm$$

$$\Delta W_{upper} = -0.02665mm,\ \Delta W_{below} = 0.02664mm,$$

$$\Delta L_{upper} = 0.23987mm,\ \Delta L_{below} = -0.23978mm \tag{2.34}$$

$$h' = 1.5899997mm,\ \ \varepsilon_h = 1.887 \times 10^{-7}, h' \approx h$$

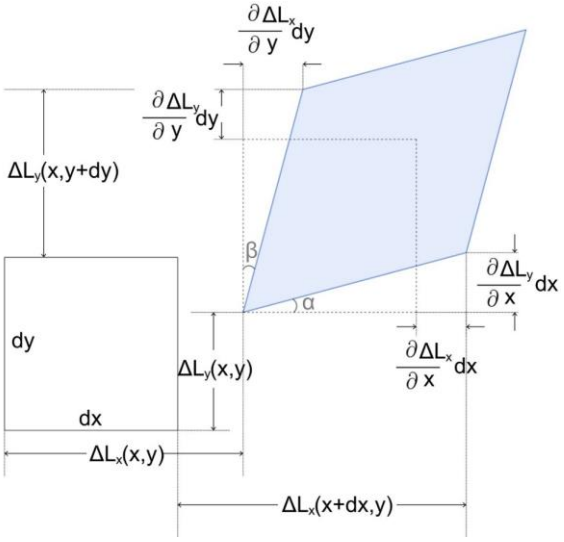

Figure 22 Illustration of engineering shear strain.

As we all know, as shown in Figure 22, the engineering shear strain is defined as,

$$\gamma_{xy} = \gamma_{yx} = \alpha + \beta = \frac{\partial \Delta L_y}{\partial x} + \frac{\partial \Delta L_x}{\partial y} \tag{2.35}$$

For this condition, combine Figure 20 and equation (2.26),

$$\gamma_{yz} = arctan\frac{1}{2}\left|\frac{\Delta W_{below} - \Delta W_{upper}}{h'}\right| \approx \frac{0.96007°}{180°}\pi \approx 0.016756$$

$$\gamma_{yz} = arctan\frac{1}{2}\left|\frac{\Delta L_{upper} - \Delta L_{below}}{h'}\right| \approx \frac{8.57746°}{180°}\pi \approx 0.149705 \tag{2.36}$$

$$\gamma_{xz} = 0$$

Then the bent beam cross section is shown in Figure 23. $h' = 1.59000mm, L = 0.79484mm; W_1 = 49.97335mm, W_2 = 50.02664mm; \frac{\Delta W'}{y} = tan0.00960° \approx 1.6755 \times 10^{-4}; \rho = 447.51539\text{mm}, \Delta\rho = 0.00016mm$. The sensitivity of the spectrum used is $1.67 \pm 0.01\mu\varepsilon$, considering equation (2.23a), the change in height can be sensed is

$$\Delta\varepsilon = \frac{\Delta y}{\rho}, \Delta y \sim 1 \times 10^{-3}mm \tag{2.37}$$

So, based on equation (2.37), the parameters for trapezoidal cross section in Figure 23 are $h' = 1.590mm, \rho = 447.515\text{mm}, r_i = 446.721\ mm, \text{L} = 0.794\text{mm}.$

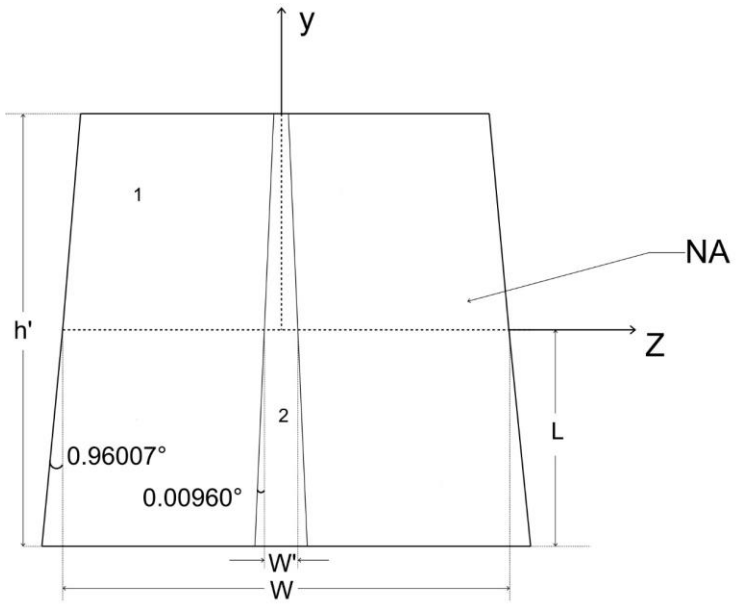

Figure 23 Cross-section for bent beam.

2.3.3 Neutral Axis Location for Beam Under Moment Load

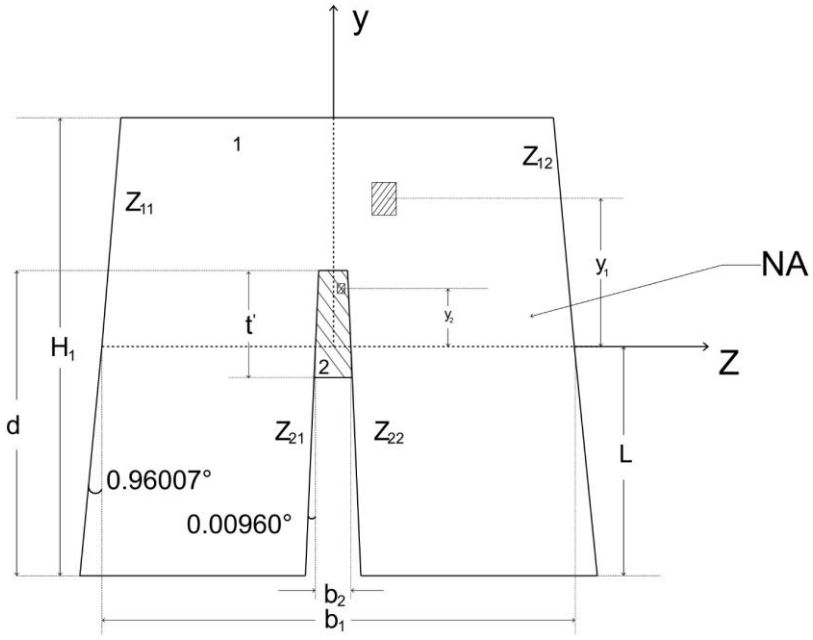

Figure 24 Cross-section for beam with a groove inside.

The dip angles of the waists of the cross section after bending are 0.96007° and 0.00960°, as shown in Figure 24. Assume the distance between top a Neutral axis location d neutral axis (NA) is L, setting NA as the z-axis. Equilibrium of force in x-direction and boundary condition,

$$\sum F_x = 0 = \iint_{A_1} \sigma_1 dA_1 + \iint_{A_2} \sigma_2 dA_2$$

$$z_{11} = 0.016758y - 25; z_{12} = -0.016758y + 25; \tag{2.38}$$

$$z_{21} = 1.6755 \times 10^{-4} y - 0.25; z_{22} = -1.6755 \times 10^{-4} y + 0.25$$

Applying equation (2.29) and $dA_1 = dy_1 dz, dA_2 = dy_2 dz$,

$$\int_{d-L}^{H_1-L} \int_{z_{11}}^{z_{12}} \frac{E'_1 y}{\rho} dz\, dy + 2 \int_{-L}^{d-L} \int_{z_{22}}^{z_{12}} \frac{E'_1 y}{\rho} dz\, dy + \tag{2.39}$$

$$\int_{d-L-t'}^{d-L}\int_{z_{21}}^{z_{22}}\frac{{E'}_2 y}{\rho}\,dz\,dy = 0$$

Integrate and rearrange,

$$\begin{gathered}\left[-0.033516(H_1-d)L^2-\left(50(H_1-d)L-0.033516\left({H_1}^2-d^2\right)L-25\left({H_1}^2-d^2\right)+0.011172\left({H_1}^3-d^3\right)\right)\right]+\\ 2[-0.01659dL^2-(49.5dL-0.01659d^2L-24.75d^2+0.00553d^3)]+\\ \frac{{E'}_2}{{E'}_1}\left[-0.000335t'L^2-\left(50t'L-0.000335\left(2dt'-t'^2\right)L-25\left(2dt'-t'^2\right)+0.000112\left(t'^3-3dt'^2+3d^2t'\right)\right)\right]=0\end{gathered} \tag{2.40}$$

For this four-point bending specimen, $E_1 = 2.9\times10^8 psi, E_2 = 1747.3 \pm 275.67 psi$, $\nu_1 = 0.3$, $\nu_2 = 0.69 \pm 0.123$, ${E'}_1 = 3.1510\times10^8 psi$, ${E'}_2 = 1099.613 \pm 274.433 ps, \frac{{E\prime}_2}{{E\prime}_1} = 3.4897 \pm 0.8709\times10^{-6} \ll 1$. The third term in equation (2.40a) is ignored. Rearrange,

$$\mathrm{M}L^2 + \mathrm{NL} + \mathrm{Q} = 0$$

$$\begin{cases} M = 0.000349 - 0.033516H_1 \\ N = 0.033156{H_1}^2 - 50H_1 + 0.519637 \\ Q = -0.011172{H_1}^3 + 25{H_1}^2 - 0.270274 \end{cases} \tag{2.41a}$$

$$\mathrm{L} = \frac{N - \sqrt{N^2 - 4MQ}}{-2M}$$

The parameters are $H_{10} = 1.59mm, \mathrm{d} = 1.04mm, \mathrm{t}' = 0.53mm, b_1 = 50mm, b_2 = 0.5mm$,

$$\mathrm{L} = \frac{N - \sqrt{N^2 - 4MQ}}{-2M} \tag{2.41b}$$

Recall $H_1 \in [1.04mm, 1.59mm]$, substituting back to equation (2.41a),

$$\frac{4MQ}{N^2} \sim 10^{-3} \ll 1 \tag{2.41c}$$

Use Taylor expansion to equation (2.41b),

$$\mathrm{L} \approx \frac{N - N\left(1 - \frac{1}{2}\frac{4MQ}{N^2}\right)}{-2M} = \frac{-Q}{N}$$

$$\mathrm{L} = \frac{25{H_1}^2 - 0.011172{H_1}^3 - 0.270274}{50H_1 - 0.033156{H_1}^2 - 0.519637} \tag{2.42}$$

$$\approx \frac{H_1}{2}\left(1 - \frac{0.011172{H_1}^3 + 0.270274}{25{H_1}^2}\right)\left(1 + \frac{0.033156{H_1}^2 + 0.519637}{50H_1}\right)$$

For $H_1 \in [1.04mm, 1.59mm]$, $\frac{0.011172{H_1}^3+0.270274}{25{H_1}^2} \in [0.01,0.035]$ and $\frac{0.033156{H_1}^2+0.519637}{50H_1} \in [0.011,0.02]$ are small terms. So $\frac{0.011172{H_1}^3+0.270274}{25{H_1}^2}\frac{0.033156{H_1}^2+0.519637}{50H_1}$ is a second order small term can be ignored.

$$\approx \frac{H_1}{2}\left(1 + 0.000216H_1 - \frac{0.010811}{{H_1}^2} + \frac{0.010393}{H_1}\right)$$

$$= \frac{H_1}{2} - \frac{0.005}{H_1} + 0.005 \tag{2.43}$$

For $H_1 = t = 1.59mm$, L =0.797mm. Without considering groove, it's 0.794mm.

$$\Delta\varepsilon = \frac{0.003}{\rho} = 6.7\mu\varepsilon \tag{2.44}$$

2.3.4 Neutral Axis Location for Composite Beams Under Moment Load

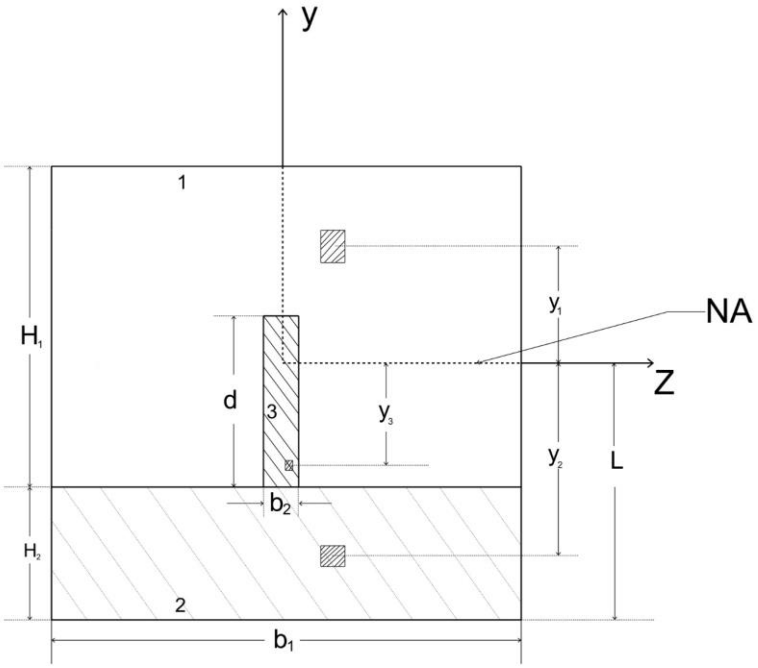

Figure 25 Cross-section for Composite Beams.

For composite beams, in order to get a rough idea of NA, the deformation change on cross section is ignored, as shown in Figure 25.

$$\sum F_x = 0 = \iint_{A_1} \sigma_1 dA_1 + \iint_{A_3} \sigma_3 dA_3 + \iint_{A_2} \sigma_2 dA_2 \tag{2.45}$$

Applying equation (2.29) and $dA_1 = dy_1 dz, dA_2 = dy_2 dz$,

$$\int_{-\frac{b_2}{2}}^{\frac{b_2}{2}} dz \int_{d+H_2-L}^{H_1+H_2-L} \frac{E'_1 y_1}{\rho} dy_1 + 2\int_{\frac{b_2}{2}}^{\frac{b_1}{2}} dz \int_{H_2-L}^{H_1+H_2-L} \frac{E'_1 y_1}{\rho} dy_1 \tag{2.46}$$

$$+ \int_{-\frac{b_2}{2}}^{\frac{b_2}{2}} dz \int_{H_2-L}^{d+H_2-L} \frac{E'_3 y_3}{\rho} dy_3 + \int_{-\frac{b_1}{2}}^{\frac{b_1}{2}} dz \int_{-L}^{H_2-L} \frac{E'_2 y_2}{\rho} dy_2 = 0$$

Integrate and rearrange,

$$\frac{H_1^2+2(H_2-L)H_1}{2}-\frac{b_2}{b_1}\frac{d^2+2(H_2-L)d}{2}+\frac{b_2}{b_1}\frac{E'_3}{E'_1}\frac{d^2+2(H_2-L)d}{2}+\frac{E'_2}{E'_1}\frac{H_2^2-2LH_2}{2}=0$$

$$\mathrm{L}=\frac{1}{2}\frac{H_1^2+2H_1H_2+\frac{E'_2}{E'_1}H_2^2+(\frac{E'_3}{E'_1}-1)\frac{b_2}{b_1}(d^2+2H_2d)}{H_1+\frac{E'_2}{E'_1}H_2+(\frac{E'_3}{E'_1}-1)\frac{b_2}{b_1}d} \tag{2.47}$$

For condition $(\frac{E\prime_3}{E\prime_1}-1)\frac{b_2}{b_1}d \ll H_1+\frac{E\prime_2}{E\prime_1}H_2$, $(\frac{E\prime_3}{E\prime_1}-1)\frac{b_2}{b_1}(d^2+2H_2d) \ll H_1^2+2H_1H_2+\frac{E\prime_2}{E\prime_1}H_2^2$, we have

$$\mathrm{L}\approx\frac{1}{2}\frac{H_1^2+2H_1H_2+\frac{E'_2}{E'_1}H_2^2+(\frac{E'_3}{E'_1}-1)\frac{b_2}{b_1}(d^2+2H_2d)}{H_1+\frac{E'_2}{E'_1}H_2}(1-\frac{(\frac{E'_3}{E'_1}-1)\frac{b_2}{b_1}d}{H_1+\frac{E'_2}{E'_1}H_2}) \tag{2.48}$$

$$\approx\frac{1}{2}(\frac{H_1^2+2H_1H_2+\frac{E'_2}{E'_1}H_2^2}{H_1+\frac{E'_2}{E'_1}H_2}+\frac{(\frac{E'_3}{E'_1}-1)\frac{b_2}{b_1}(d^2+2H_2d)}{H_1+\frac{E'_2}{E'_1}H_2})(1-\frac{(\frac{E'_3}{E'_1}-1)\frac{b_2}{b_1}d}{H_1+\frac{E'_2}{E'_1}H_2})$$

Ignore second-order small term,

$$\mathrm{L}\approx\frac{1}{2}\frac{H_1^2+2H_1H_2+\frac{E'_2}{E'_1}H_2^2}{H_1+\frac{E'_2}{E'_1}H_2}(1-\frac{(\frac{E'_3}{E'_1}-1)\frac{b_2}{b_1}d}{H_1+\frac{E'_2}{E'_1}H_2})+\frac{(\frac{E'_3}{E'_1}-1)\frac{b_2}{b_1}(d^2+2H_2d)}{H_1+\frac{E'_2}{E'_1}H_2} \tag{2.49}$$

Ignore first-order small term,

$$\mathrm{L}\approx\frac{1}{2}\frac{H_1^2+2H_1H_2+\frac{E'_2}{E'_1}H_2^2}{H_1+\frac{E'_2}{E'_1}H_2} \tag{2.50}$$

Furthermore, for $\frac{E\prime_2}{E\prime_1}\frac{H_2}{H_1} \ll 1$,

$$\mathrm{L}\approx\frac{H_1^2+2H_1H_2+H_2^2\frac{E'_2}{E'_1}}{2H_1}\left(1-\frac{E'_2}{E'_1}\frac{H_2}{H_1}\right) \tag{2.51}$$

$$L \approx \frac{H_1}{2} + H_2 - \frac{H_1 + H_2}{2} \cdot \frac{E'_2}{E'_1} \frac{H_2}{H_1}$$

For simplification, we treat

$$L \approx \frac{H_1}{2} + H_2 \tag{2.52}$$

2.3.5 Four-point Load Specimen

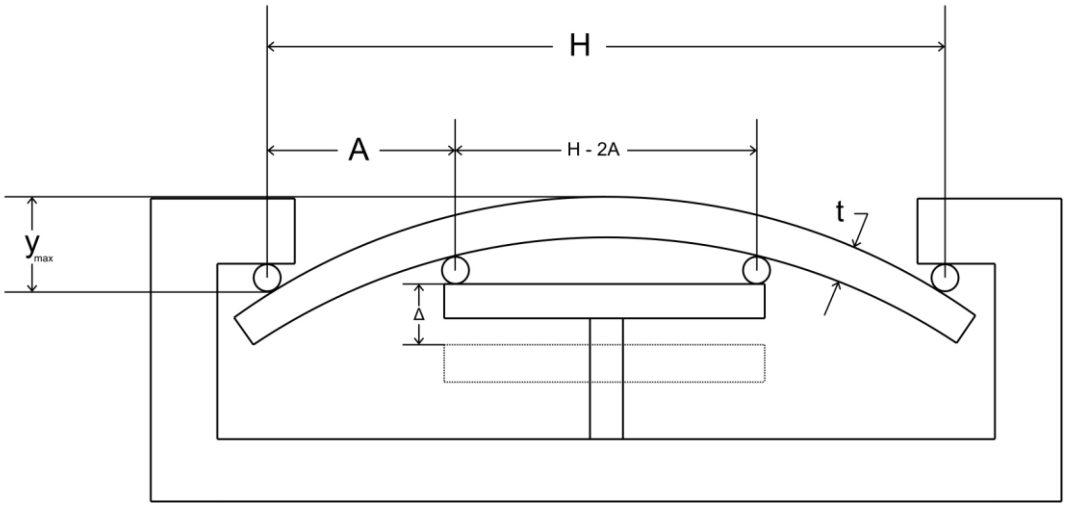

Figure 26 Four-point loaded model.

This model [46] can be applied to any metal stressed under elastic limit. The specimen holder, shown in Figure 26, should be strong enough to retain the applied stress. This specimen shall be typically 25mm to 51mm wide and 127mm to 254mm long [46]. The two inner supports should be located symmetrically around midpoint. With small deflections ($\frac{y_{max}}{H}$ less than 0.1), the elastic stress for midportion of the specimen in the outer fibers is [46]

$$\varepsilon_{max} = \frac{\sigma_{max}}{E} = \frac{12t \cdot y_{max}}{3H^2 - 4A^2} \tag{2.53}$$

, where t is the thickness of metal plate; y is maximum deflection between outer supports; H is distance between outer supports; A is distance between inner support and closest outer support. The radius of curvature ρ for such model is [46],

$$\rho = r_i + \frac{t}{2} = \frac{\sqrt{\Delta^2 + A^2}(H - 2A)}{2\Delta} + \frac{t}{2} \tag{2.54}$$

The strain based on the distance the inner supports go up, Δ, is

$$\varepsilon = \frac{y}{\rho} = \frac{y}{446.721 + \frac{t}{2}} \tag{2.55}$$

For small deflections ($\Delta \ll H, \Delta \ll H - 2A$),

$$\varepsilon \approx 0.0022385\mathrm{y}(1 - \frac{t}{893.442}) \tag{2.56}$$

, where y is the distance between measurement point and NA.

All calculations are based on the corrosion going on before the embedded fiber exposed. The parameters chosen for our four-point bending model are $\mathrm{A} = 27\mathrm{mm}, \mathrm{H} = 120\mathrm{mm}, \Delta =$ 2mm.

2.3.5.1 Instant Bending Strain Rate Analysis During Corrosion without Coating

Position for FBG is, as shown in Figure 24,

$$\mathrm{y} = \mathrm{d} - \mathrm{L} \tag{2.57}$$

Combine equation (2.23a), (2.57) and (2.43) together,

$$\begin{aligned} \varepsilon &\approx 0.0022385(1.0395 - \frac{H_1'}{2} + \frac{0.005}{H_1'})(1 - \frac{H_1'}{893.442}) \\ &= 0.0022385(1.0395 - 0.5012H_1' + \frac{0.005}{H_1'} + \frac{H_1'^2}{1786.884}) \end{aligned} \tag{2.58}$$

For $H_1' \in [1.04,1.59]$, $\frac{0.005}{H_1'} \in [3 \times 10^{-3}, 5 \times 10^{-3}]$, $\frac{H_1'^2}{1786.884} \in [0.6 \times 10^{-3}, 1.5 \times 10^{-3}]$, sensitivity is $\sim 1.67 \pm 0.01\mu\varepsilon$, so remain the average value for this two terms,

$$\begin{aligned} \varepsilon &\approx 0.0022385(1.0395 - 0.5012H_1' + 0.004 \pm 0.0005 + 0.001 \pm 0.0002) \\ &= 0.0022385(1.0400 - 0.5012H_1') \pm 1.2\mu\varepsilon \\ &= 2328\mu\varepsilon - 1.1219 \times 10^{-3}H_1' \pm 1.2\mu\varepsilon \end{aligned} \tag{2.59}$$

Assume corroded thickness is X(t)

$$\varepsilon(\mathrm{t}) \approx 2328\mu\varepsilon - 1.1219 \times 10^{-3}(H_1 - \mathrm{X(t)}) \pm 1.2\mu\varepsilon \tag{2.60}$$

Take derivation,

$$\frac{d\varepsilon(t)}{dt} \approx 1.1219 \times 10^{-3} \cdot \frac{dX(t)}{dt} \tag{2.61}$$

The corrosion speed will be,

$$\mathrm{v(t)} \approx 891 \cdot \frac{d\varepsilon(\mathrm{t})}{dt} \propto \frac{d\varepsilon(\mathrm{t})}{dt} \tag{2.62}$$

The corrosion speed is in direct proportion to the rate of strain change. So, the rate of strain change is positive if the thickness of plate keeps decreasing during corrosion.

2.3.5.2 Instant Bending Strain Rate Analysis During Corrosion with a Coating Layer

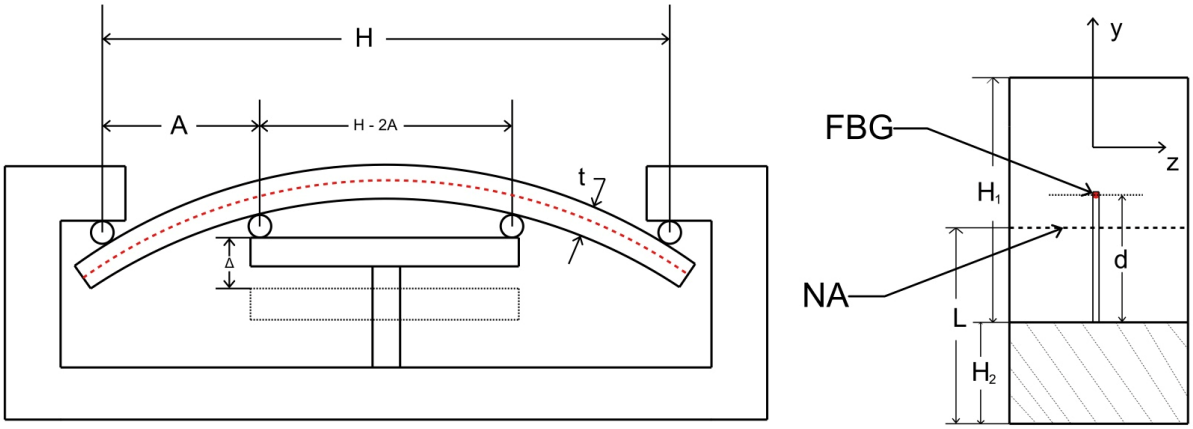

Figure 27 Illustration for the four-point bending model with FBG embedded in.

Assume the speeds of corrosion at different places where suffer same strain, are same value and the corrosion only happen from the top of material 1. The depth of the groove is $\mathrm{d} = 0.8\mathrm{mm}$ and the thickness between the fiber and the bottom of the groove is negligible.

The distance between measurement point and NA is,

$$\mathrm{y} = \mathrm{d} - \mathrm{L} + H_2 \tag{2.63}$$

If the first order of $\frac{\boldsymbol{H_2}}{\boldsymbol{H_1}}\frac{\boldsymbol{E'_2}}{\boldsymbol{E'_1}}$ is small enough to be ignored, equation (2.52) can be applied to equation (2.63). During corrosion, assuming the corroded thickness is a function of time X(t), the strain becomes,

$$\varepsilon(\mathrm{t}) \approx 0.0022385 \cdot (\mathrm{d} - \frac{H_1 - \mathrm{X(t)}}{2}) \tag{2.64}$$

Here the thickness t, in the term calculated for the radius of curvature ρ, is a constant during corrosion. Because the inner and outer supports are fixed, the change of the location of NA compared to the radius of curvature ρ is small enough to be ignored.

Take the derivative with respect to time,

$$\frac{d\varepsilon(\mathrm{t})}{dt} \approx 1.1219 \times 10^{-3} \cdot \frac{dX(\mathrm{t})}{dt} \tag{2.65}$$

If the corrosion speed is v(t),

$$\mathrm{v(t)} \approx 891 \cdot \frac{d\varepsilon(\mathrm{t})}{dt} \propto \frac{d\varepsilon(\mathrm{t})}{dt} \tag{2.66}$$

Equation (2.66) is totally same to results without coating layer.

If the first order of $\frac{\boldsymbol{H_2}}{\boldsymbol{H_1}}\frac{\boldsymbol{E'_2}}{\boldsymbol{E'_1}}$ cannot be ignored, equation (2.51) should be applied to equation (2.63). The strain becomes,

$$\varepsilon(\mathrm{t}) \approx 0.0022385 \cdot (\mathrm{d} - \frac{H_1 - \mathrm{X(t)}}{2} + \frac{H_2 \frac{E'_2}{E'_1}}{H_1 - \mathrm{X(t)}} \cdot \frac{H_1 - \mathrm{X(t)} + H_2}{2}) \tag{2.67}$$

At the beginning of the corrosion, the corroded thickness X(t), is a small term compared to H_1, keeping the first order term,

$$\approx 0.0022385 \cdot [\mathrm{d} + \frac{\frac{E'_2}{E'_1}H_2 - H_1 + \frac{H_2}{H_1}\frac{E'_2}{E'_1}H_2}{2} + (1 + \frac{H_2}{H_1}\frac{E'_2}{E'_1}H_2)\frac{\mathrm{X(t)}}{2}] \tag{2.68}$$

Take the derivative with respect to time and set the corrosion speed as v(t),

$$\mathrm{v(t)} \approx 891 \cdot (1 + \frac{H_2}{H_1}\frac{E'_2}{E'_1}H_2) \cdot \frac{d\varepsilon(\mathrm{t})}{dt} \propto \frac{d\varepsilon(\mathrm{t})}{dt} \tag{2.69}$$

With the corrosion going on, the corroded thickness X(t), is not small. The left thickness of material at time t, $H'_1(t)$.

$$\frac{d\varepsilon(\mathrm{t})}{dt} \approx 0.0022385 \cdot \frac{\frac{H'_1(t)^2}{2} + H_2\frac{E'_2}{E'_1}H'_1(t) + \frac{H_2}{2}H_2\frac{E'_2}{E'_1}}{[H'_1(t) + H_2\frac{E'_2}{E'_1}]^2} \cdot \frac{dX(\mathrm{t})}{dt} \tag{2.70}$$

$$\mathrm{v(t)} \approx 891 \frac{[H_1'(t) + H_2 \frac{E'_2}{E'_1}]^2}{H_1'(t)^2 + 2\frac{E'_2}{E'_1} H_2 H_1'(t) + \frac{E'_2}{E'_1} {H_2}^2} \cdot \frac{d\varepsilon(\mathrm{t})}{dt} \propto \frac{d\varepsilon(\mathrm{t})}{dt} \tag{2.71}$$

The corrosion speed is still in direct proportion to the rate of strain change. So, the rate of strain change is always positive if the thickness of plate keeps decreasing during corrosion, whatever there is a coating layer on the bottom face or not.

3.0 Experiment Design

The main purpose for this experiment is to monitor the corrosion process of a carbon steel plate under 4-point bending in 3.5% NaCl solution. The main idea is that the strain introduced by 4-point bending will change during the corrosion. Measure this strain change during corrosion and plot it against time to find some regularity. However, as we all know, the residual strain in the carbon steel cannot be ignored or eliminated. In order to study and minimize the residual strain influence, we set two experiments under same corrosion condition but without bending. One plate is totally same, and another plate has different width. We hope to find a proper way to process the data from three experiments to figure out the strain only changed by bending. In case, we also set a bare FBG in same temperature environment to wipe off the temperature influence.

3.1 Preparation

The low-carbon steel plates used are Low-Carbon Steel Bars with Rounded Edges, supplied by McMaster Inc. The Material composition are 98.06-99.42% Iron, 0.13-0.20% Carbon, 0.30-0.90% Manganese, 0.04% Max Phosphorus, 0.15-0.30% Silicon, 0.50% Max Sulfur. Coefficient of thermal expansion is 7.1×10^{-6}.

3.1.1 First Experiment

3.1.1.1 Low-carbon Steel Plates with FBG Embedded in and B-4811 Layer on same Side

The low-carbon flat plates are all 3 cm in width and 1.59 mm in thickness. Each one has a groove in the mid, 0.8 mm in depth and 500 μm in width, as shown in Figure 28(b). Embed the FBG at the mid-point of the plate with groove fully filled by B-45TH, curing at 90℃ for 4 hours. Use knife to remove the adhesive out of the groove when curing start for 1hour. Then paint the B-4811 on the side of the bar where the groove is open, as uniform as possible. Cure at 90℃ for 5 hours, as shown in Figure 29.

(a)

(b)

Figure 28(a) FBG locates in the middle of the black mark, 10mm long; (b) Embed an FBG in the low-carbon flat bar with B-45TH fully filled in the groove, curing at 90℃ for 4 hours.

Figure 29 low-carbon plate with FBG embedded in and anti-corrosion adhesive layer at one side.

3.1.2 Second Experiment

3.1.2.1 Low-carbon Steel Plates with Embed FBG in, no Adhesive on any Side

The low-carbon flat plates are all 13.5cm in length and 1.59 mm in thickness. Two of them are 5 cm in width and the left is 3 cm inches. Each one has a groove in the mid , 1.04 mm in depth and 500 μm in width, as shown in Figure 30(b). The FBG is located at the mid-point of the length. After using small piece rubber to fix the fiber at two ends, embed the FBG at the mid-point of the plate by partly filled by B-45TH. In order to transfer the strain perfectly through the adhesive layer, the B-45TH adhesive layer is only 4cm long, about half of the depth of the groove in thickness at the mid. Use small needle to remove half of the adhesive during curing process, try to make the adhesive layer not too thick. In order to reduce the strain caused by gravity of fiber, there are 4 points with a nearly 2mm long B-45TH adhesive layer at two side to fix the fiber in the groove. Use knife to remove the adhesive out of the groove. Then fully cure at 90℃ for 4hours.

(a) 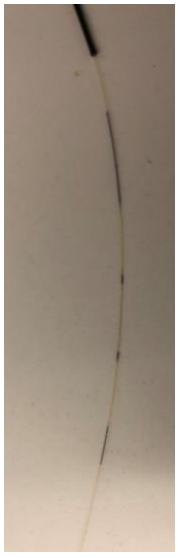 (b) 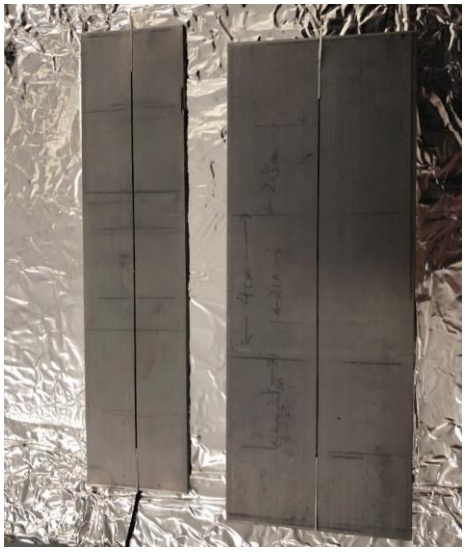

Figure 30(a) FBG locates in the middle of the black mark, 10mm long; (b) Embed an FBG in the low-carbon flat bar with B-45TH partly filled in the groove, curing at 90℃ for 4 hours.

3.2 Four-point Bending Specimen

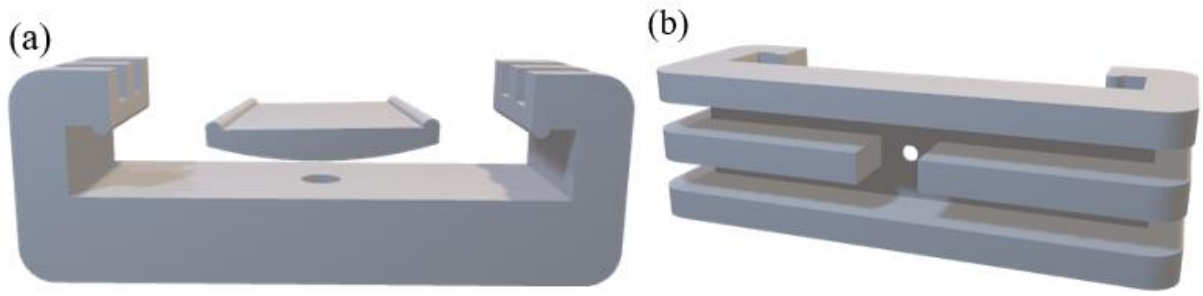

Figure 31 SolidWork model for four-point bending specimen. (a) Front view; (b) Bottom view.

The four-point bending model is drawn by SolidWorks, as shown in Figure 31. In order to make sure the holder strong enough that would withstand the influence of the applied bending shear force without deterioration or change in shape, two grooves are designed to deal with it, as shown in Figure 31(b). The hole left in the mid of the holder is used to allow the screw through. The position adjustment of the inner support plate is controlled by the screw. The four-point bending specimen is built by 3-D print technique in Machine Shop and shown in Figure 32 in kind.

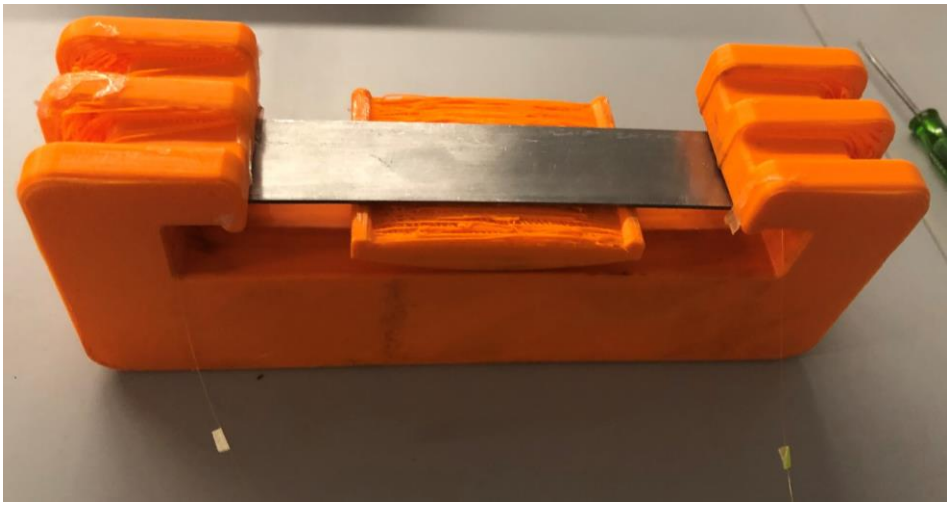

Figure 32 Four-point bending specimen with low-carbon steel installed on, with screw upward 2.5mm.

3.3 System Preparation and Experiment Set Up

3.3.1 Optic Fiber Measurement System

The equipment used for this experiment are shown in Figure 33. The fiber with 5 FBGs is produced by MICRON OPTICS Inc. The Optical Spectrum Analyzer is AQ6374 Wide Range 350-1750nm, YOKOGAWA Inc. Fiber Optic Circulator is a three-port device that allows light to travel in only one direction, separating the reflected light from mixed signal.

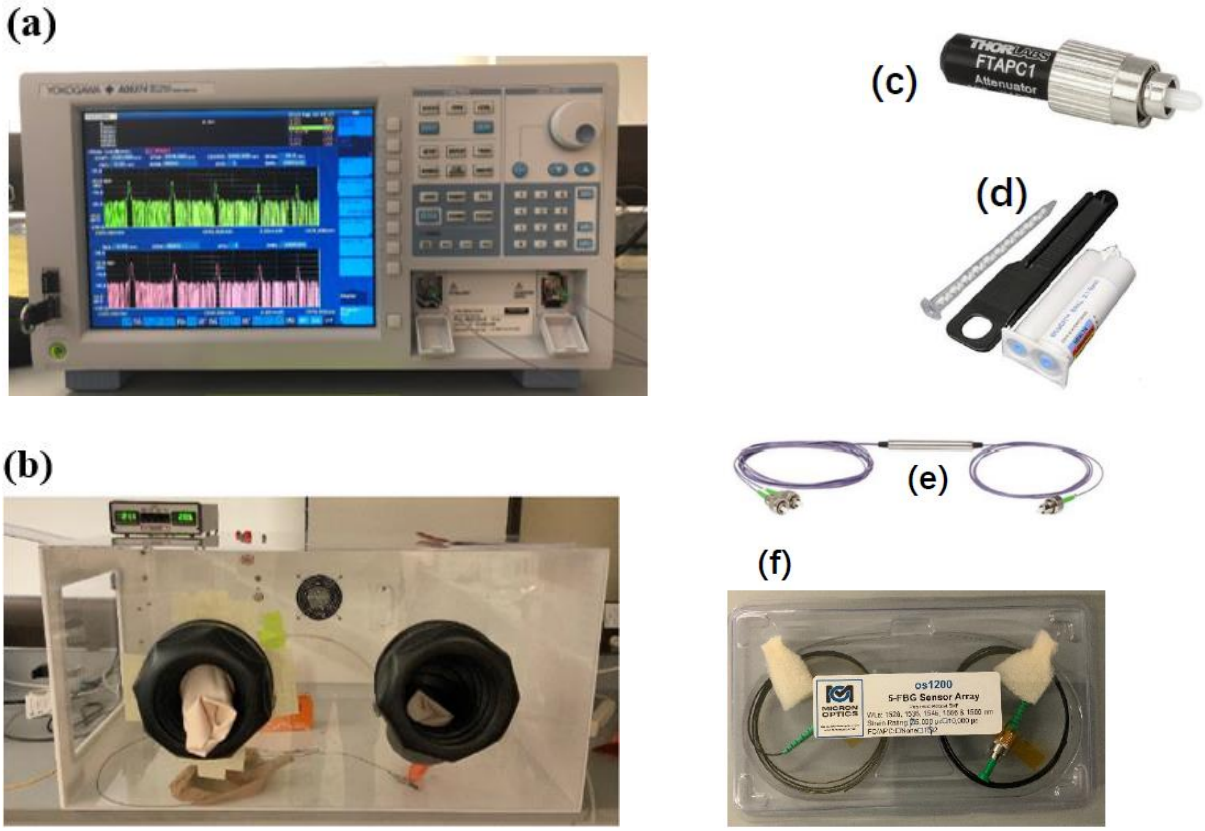

Figure 33Measurement system and components for setting up the FBG sensor measurement. (a) AQ6374 Optical Spectrum Analyzer, YOKOGAWA; (b) Chamber used for corrosion; (c) Fiber Optic Light Trap, Thorlabs Inc; (d) B-45TH adhesive for carbon steel and polyimide, B-4811 adhesive for coating layer; (e) Fiber Optic Circulator 1525-1610 nm SMF FC/APC, Thorlabs Inc; (f) OS1200-optic fiber with 5 FBGs, MICRON OPTICS.

3.3.2 Experiment Set Up

3.3.2.1 First Experiment

The low-carbon steel plate is first installed on the four-point bending specimen, as shown in Figure 32 before. Then put the four-point bending specimen and the reference carbon steel plate in the white box, filled with 3.5% NaCl solution, as shown in Figure 34(a). Put a soft tube into solution, connected with a low speed air source. Put the corrosion monitoring system in the chamber. Then connect the fiber to the optic circulator and optic spectrum analyzer.

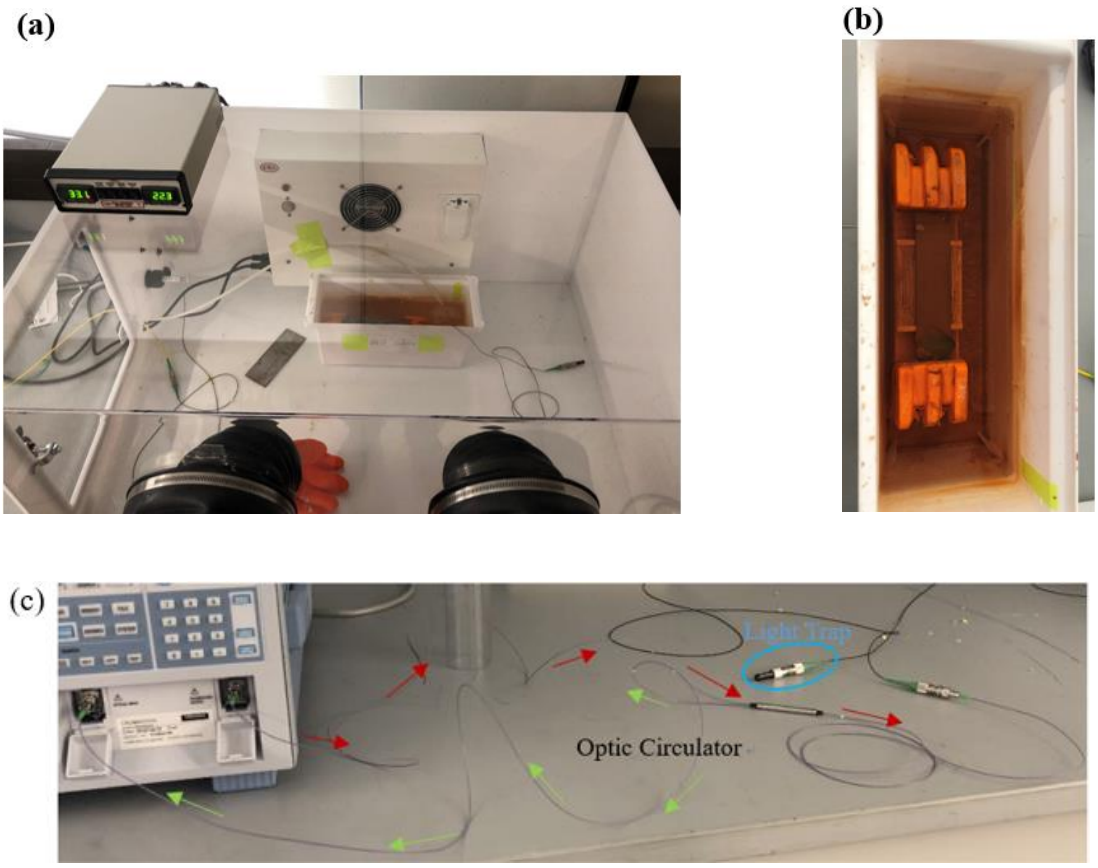

Figure 34 Corrosion monitoring system. (a) Corrosion monitoring system; (b) Four-point bending model corrodes for several days; (c) Analyzer and the principle diagram for optic circulator.

3.3.2.2 Second Experiment

Based on the failure of the first experiment, instead of preventing corrosion in NaCl solution, partial corrosion is chosen. The side with groove sets towards the inner support element and install a cover above the plate, as shown in Figure 35. This special cover made by light thin copper sheet is bonded on the carbon steel plate by B-45TH. The low-carbon plate with FBG embedded in is first installed on four-point bending model and then bonded with this cover. As to the two references, they are also bonded with same copper cover. After the B-45TH fully cured, the 3.5% NaCl solution is put in the cover and refreshed every 3days. The copper covers shown in Figure 35(a) and Figure 35 (c) are all 5.68g. The copper cover in Figure 35(b) is 5.04g.

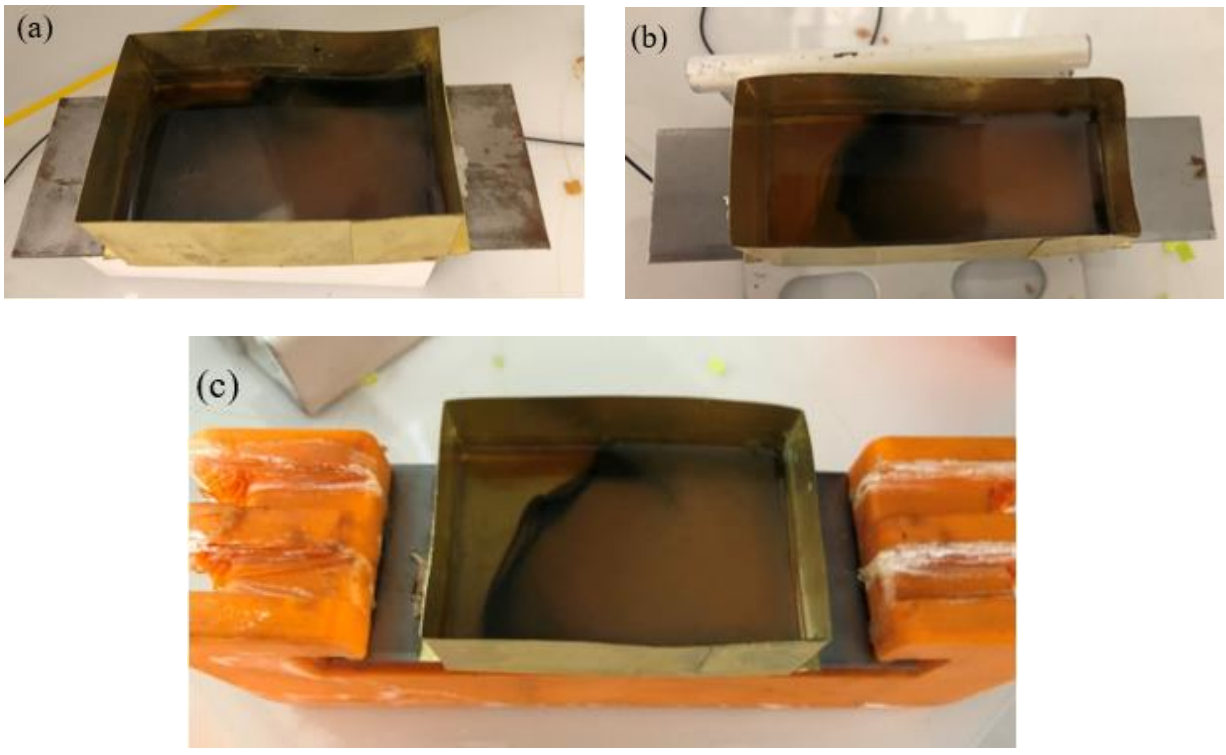

Figure 35 Corrosion models: (a) Reference 1; (b) Reference 2; (c) Four-point bending specimen with low-carbon flat plate installed on.

4.0 Results and Discussion

Now that all experiment preparations are completed, the data should be processed following these steps. First, set a reference state, simply because the strain and Bragg wavelength change needing a reference value. Second, remove the temperature term though subtracting the real-time environment temperature monitoring results. Then collect the total strain change during corrosion for three experiments. Finally, by observing the results, find a proper way to analyze the data to get a result matching the theory that, the rate of strain change during time is always positive and proportional to the corrosion speed.

4.1 Reference Bragg Wavelengths of 5 FBGs

Released the fiber with 5 FBGs on in our lab and collected the data up to 200 hours. As shown in Figure 36, the equilibrium positions of $\Delta\lambda$ for each FBG are all around 0. So, take the average value as the reference Bragg wavelength, at temperature 22℃. The strains measured in the following experiments are all the relative value compared to the FBG length at 22℃, without external force. The reference Bragg wavelengths for the 5 FBGs on this fiber are 1525.201nm, 1535.2nm, 1546.063nm, 1555.978nm, 1564.963nm.

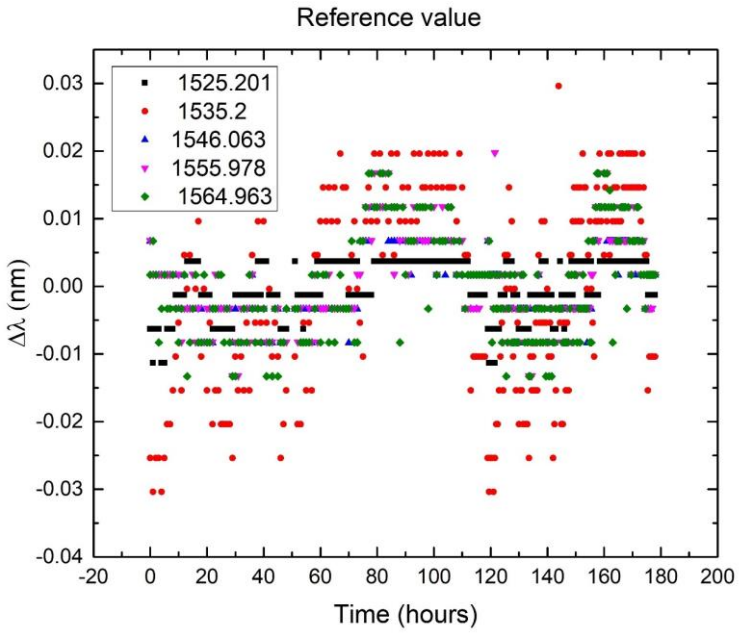

Figure 36 Results for Bragg wavelength over time. The FBG is put in lab environment, without ecternal force.

4.2 Examine the Temperature Term Coefficient

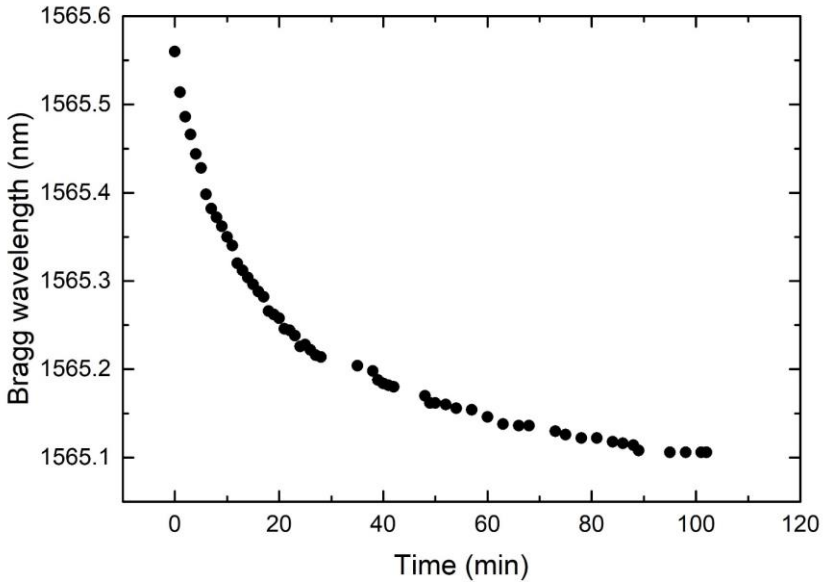

Figure 37 Result for Bragg wavelength over time during water cooling.

Put the fifth FBG into the water, letting it cool from 65℃ to 24℃. The result for the Bragg wavelength is shown in Figure 37. The classic Bragg wavelength equation for Bragg wavelength at 1564.963nm is,

$$\Delta\lambda_{Bragg} = 1220.671 \cdot \varepsilon_{FBG} + 14.32 \times 10^{-3} \cdot \Delta T \tag{4.1}$$

The fiber is tiny and sensible, so that the surface tension at the interface between the fiber and water cannot be ignored. So, the strain term cannot be ignored. Setting a reference experiment in the water undergoing same strain influence but without temperature influence is difficult, so, we choose the strain at initial time as the reference value and assume the change of this surface tension can be ignored during temperature change. Bragg wavelength equation changes into,

$$\lambda_t - \lambda_0 = 14.32 \times 10^{-3} \cdot (\mathrm{T}_t - \mathrm{T}_0) \tag{4.2}$$

However, with this equation, we cannot get the temperature change from 65℃ to 24℃. Go back to classic Bragg wavelength equation,

$$\frac{\Delta\lambda_{Bragg}}{\lambda_{Bragg}} = (1 + \rho_e)\varepsilon_{FBG} + (\alpha + \eta)\Delta T \tag{4.3}$$

Eliminating the influence of strain, the relationship between wavelength change and temperature change should be linear, as

$$\Delta\lambda_{Bragg} = k \cdot \Delta T \tag{4.4}$$

Use the initial data and final data, we get $k = 11.073 \times 10^{-3}$. Compared to the theoretical value 14.32×10^{-3}, the percentage error is up to 22.6%. This may cause by the MICRON OPTICS. When we asked them for the value for ρ_e α η, they gave us the value on the book [20]. Although these FBGs are made in hurry, they fabricated and delivered these to us in only one week. What's more, the change of strain caused by the surface tension during temperature change might be significant, contributing to this large error. Due to this big error, we set a reference sample to eliminate the temperature term in the other experiments.

Because this linear relationship, the temperature change over time is exactly same as the Bragg wavelength change, shown in Figure 37, only difference is the scale of vertical coordinates.

Rearrange the classic Bragg wavelength equation,

$$\frac{\lambda_{Bragg}{}' - \lambda_{Bragg}}{\lambda_{Bragg}} = (1 + \rho_e)\frac{L_{FBG}{}' - L_{FBG}}{L_{FBG}} + (\alpha + \eta)(T' - \mathrm{T}) \tag{4.5}$$

, where the $\lambda_{Bragg}{}'$ is the measurement value of Bragg wavelength after the FBG suffers a strain and temperature change. So, we need to confirm a reference value for the Bragg wavelength, length of FBG and temperature. For this experiment, we choose the room temperature 22℃ and release the fiber on the desk, without any strain.

With the value supplied by MICRON OPTICS, the classic Bragg wavelength equation becomes

$$\frac{\Delta\lambda_{Bragg}}{\lambda_{Bragg}} = 0.78 \cdot \varepsilon_{FBG} + 9.15 \times 10^{-6} \cdot \Delta T \tag{4.6}$$

4.3 First Experiment

The residual strain, left during forge, will have a big influence. In order to reduce this factor, another sample is cut from the same low-carbon flat bar, with the same groove on it. The first FBG was embedded in, working as a reference to measure the residual strain influence. This sample was also put in the 3.5% Nacl solution in same container. As mentioned before, the temperature coefficient term has a great error. So, the left bare FBGs are also put in the chamber to measure the environment temperature influence.

4.3.1 Unexpected Experiment Results

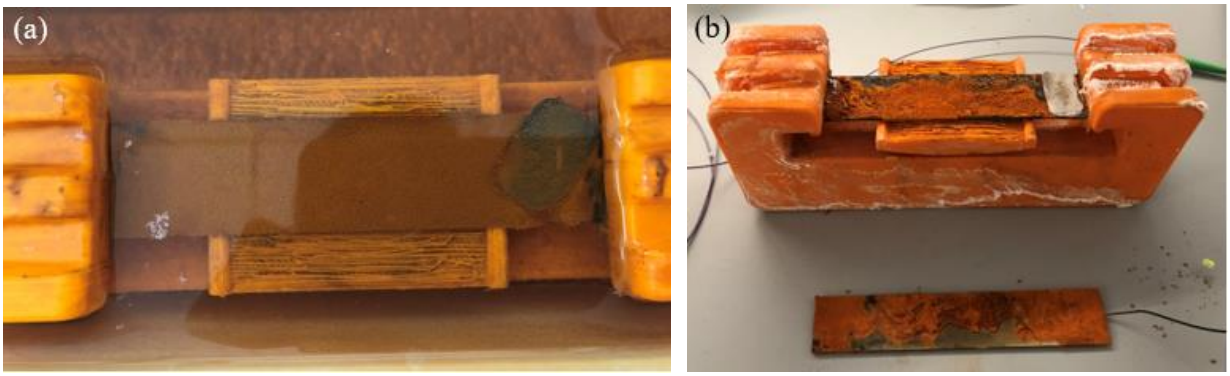

Figure 38 Pictures of the bent carbon steel plates: (a) during corrosion; (b) after corrosion.

The four-point bending corrosion model seems to process smoothly during corrosion, as shown in Figure 38(a). It looks heavily corroded. The small piece shows in Figure 38(a) is a thin copper sheet, accelerating the corrosion process. After 400 hours corrosion, the left samples are shown in Figure 38(b), many rusts left on the upper face of the carbon steel.

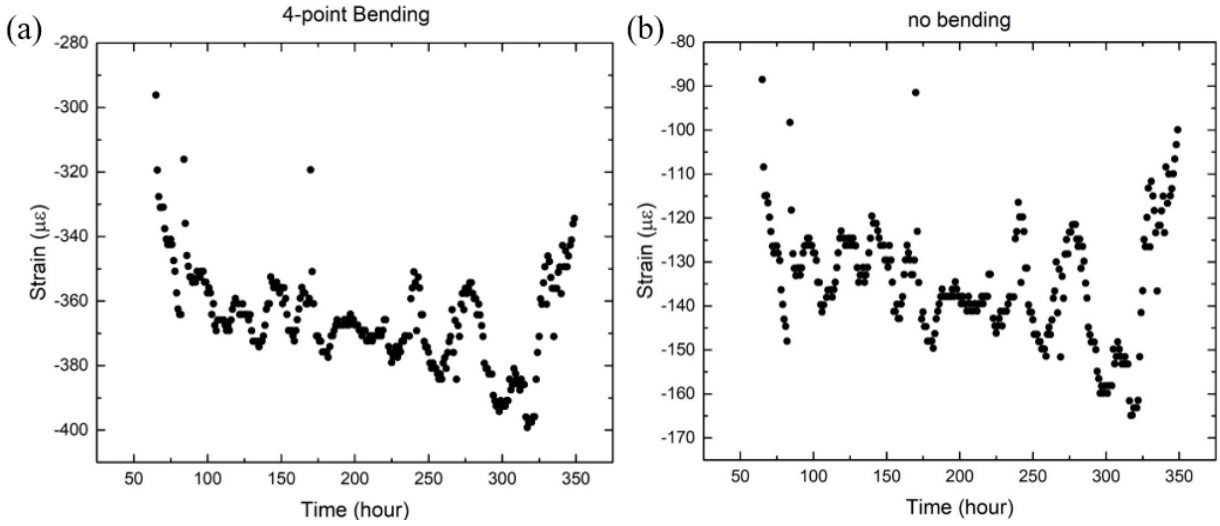

Figure 39(a) Strain change over time during corrosion for the sample under four-point bending.; (b) Strain change over time during corrosion for the sample without bending.

The results shown in Figure 39 have eliminated the temperature by setting reference sample in same temperature without external force. First, these results show one thing obviously that the FBG strain sensors are very sensitive that they can sense the strain changed by bending and residual strain release during corrosion. However, we cannot find an obvious rising tendency for any results. Even if we subtract the residual strain measured by no-bending carbon steel plate from the results measured by bending carbon steel plate, as shown in Figure 40. What's worse, we even get a downtrend, totally against our theory model.

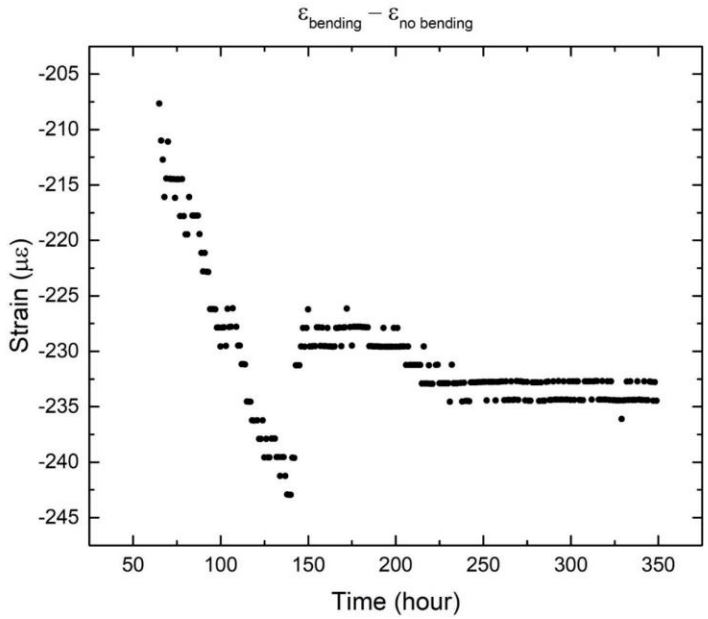

Figure 40 The strain change only caused by bending over time, by subtracting the strain meaured without bending from the result with bending.

The properly reason for this result may be the reason that the thickness of the coating layer increased during corrosion. The speed of the coating layer growing is faster that the speed of the carbon plate decreasing during corrosion. As we can see in Figure 41, the coating layer changed a lot, though it's made by a high corrosion resistant adhesive.

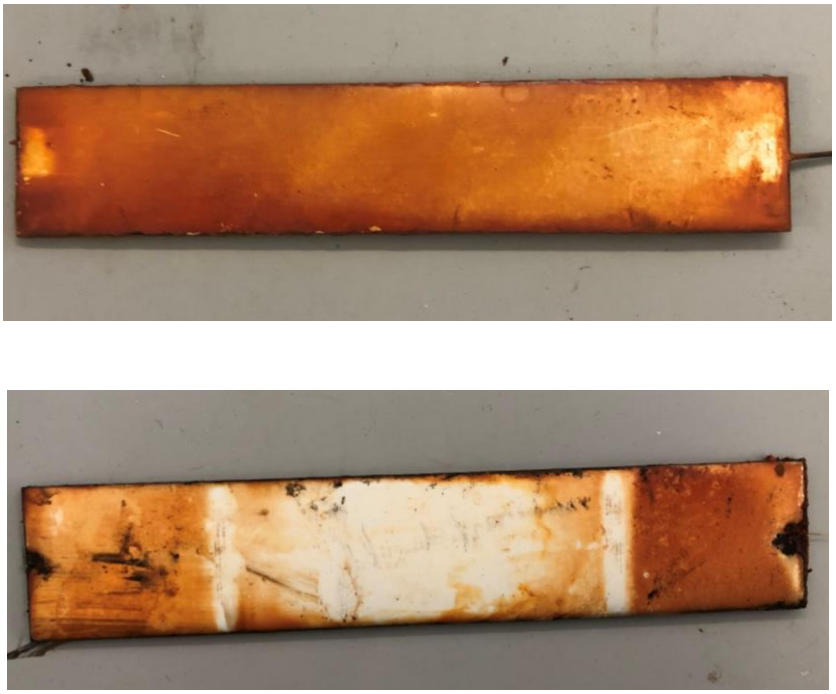

Figure 41 The coating layer made by so called high corrosion resistant changed after long time corrosion.

4.4 Second Experiment

In order to avoid the same problem caused by the coating layer influence in the former experiment, a new experiment is designed and more details about the adhesive layers are concerned. The fiber is bonded with only 4 cm long B-45TH adhesive layer around the FBG according to other's work [45]. Inside of fully filling the groove, only half of depth is filled. Inside of putting whole system into water, this time we installed a box made by copper on the front face of the carbon plate, filled with NaCl solution. We also used silver conducive epoxy to connect the copper and carbon steel plate outside the solution to form a circuit to accelerate the corrosion speed. One bare FBG remained for temperature measurement purpose and two FBG with same model except bending are set up for residual strain reference.

4.4.1 Examine the New Corrosion Model Design

In order to make sure that the fiber is bonded with only 4 cm long B-45TH adhesive layer, several marks are made besides the groove, as shown in Figure 42 (a). To bond the cover and carbon steel, the water tightness corrosion resistance of adhesives should be examined. B-45TH and B-4811 are adhesives on hand and applied to bond the copper cover, as shown in Figure 42 (b). The white adhesive layer is B-4811 and the hyaline layer is B-45TH. The results after 5 days corrosion are shown in Figure 42(c) and Figure 42(d). Without any further operation to this corrosion model, something like a grease layer will formed above the solution. After remove the solution, a black layer is deposited on the corroded carbon steel surface, probably carbon. After examining the bonding area, the B-45TH adhesive performs better than B-4811.

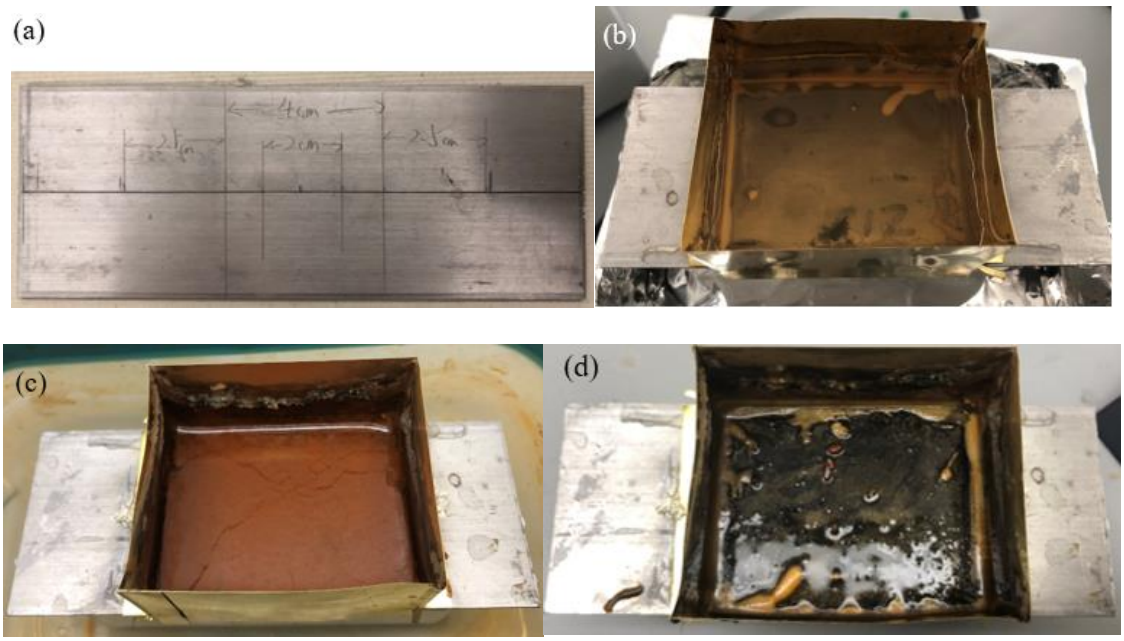

Figure 42 Examine the new corrosion model behavior. (a) Marks to help adjust the B-45TH adhesive layer; (b) Examine the water tightness corrosion resistance of two kinds of adhesives; (c) After 5 days corrosion without any further operation; (d) The carbon layer formed on the carbon steel surface during corrosion.

4.4.2 Results and Analysis of New Corrosion Model

The FBG is very sensitive to surrounding temperature change and strain change. To wipe off the temperature influence, a temperature reference is required. As shown in Figure 39, the residual strain left during forge has a big influence on the results. For purpose of analyzing and minimizing residual strain influence, two samples are set as residual strain references. One sample is totally under same condition comparing to bending model, cut from the same low-carbon steel plate in same way, but with no bending applied. Another sample has different width and from another low-carbon steel plate. These two samples are expected to have different residual strain to study the influence.

4.4.2.1 Results of Strain Change During Corrosion

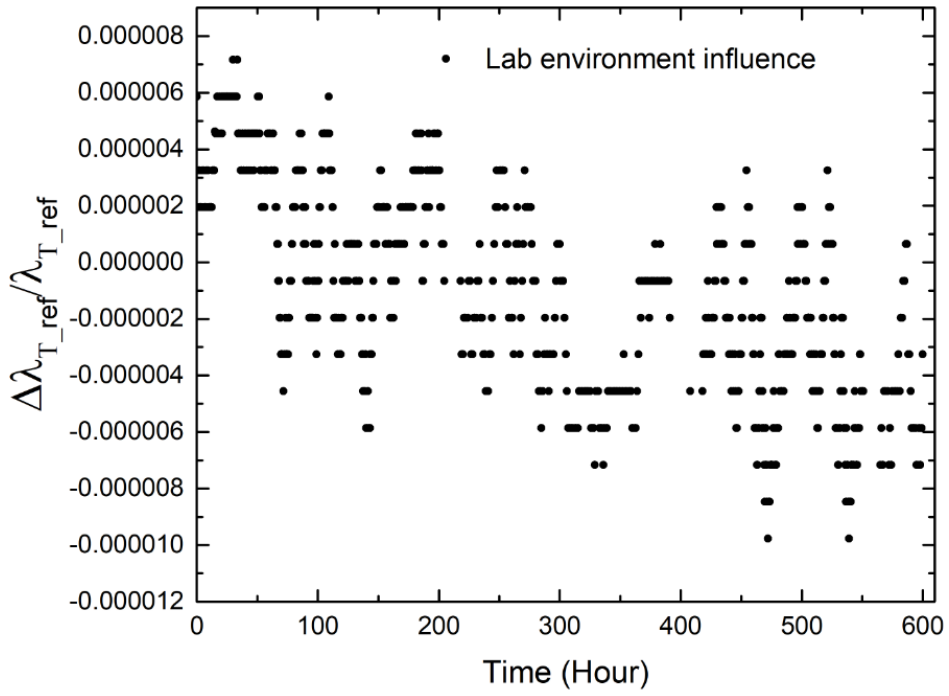

Figure 43 Lab environment temperature influence.

The result of environment temperature influence is shown in Figure 43. According to equation (4.3), $\frac{\Delta\lambda_{Bragg}}{\lambda_{Bragg}}$ is in direct proportion to ΔT without strain influence, so Figure 43 also shows the regularity of temperature change during the corrosion. The term $\frac{\Delta\lambda_{Bragg}}{\lambda_{Bragg}}$ as y-axis is for the convenience to wipe out temperature influence from later experiments' results,

$$\frac{\Delta\lambda_{sample}}{\lambda_{sample}} - \frac{\Delta\lambda_{ref}}{\lambda_{ref}} = (1 + \rho_e)\varepsilon_{FBG} \tag{4.7}$$

By applying equation (4.7) to experimental results, the total strain change can be got.

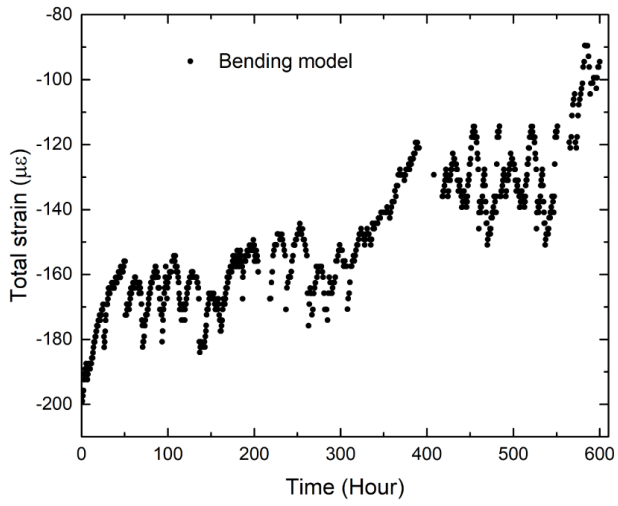

Figure 44 Total strain change for bending model during corrosion.

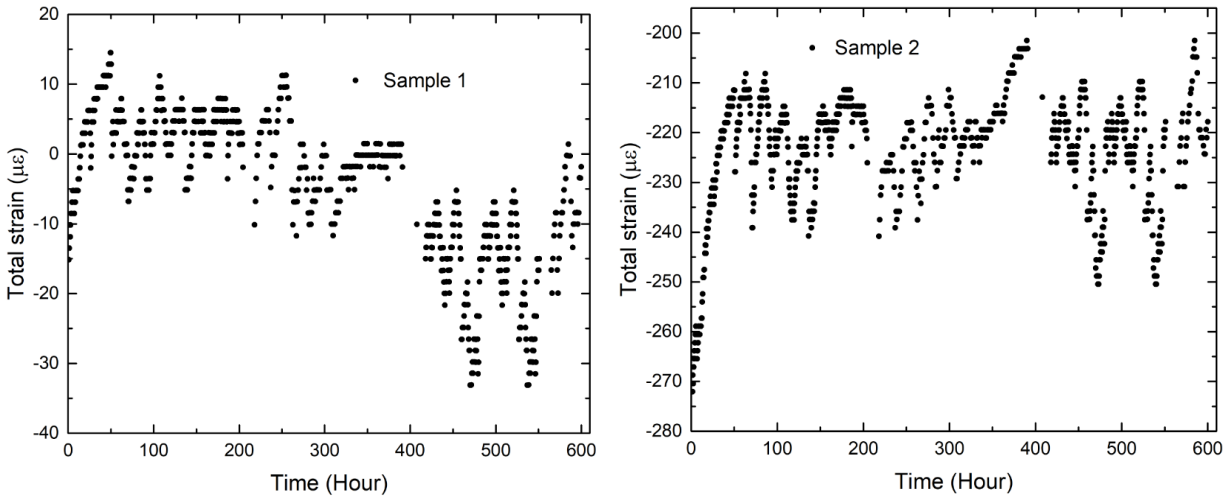

Figure 45 Total strain change for reference 1 and reference 2 during corrosion.

Figure 44 and Figure 45 show the total strain change during corrosion. It is easy to see the residual strain released during corrosion cannot be ignored. However, there is still an obvious rising tendency we can see in the bending model.

There are two possible reasons for the decline in each small cycle shape, shown in Figure 44 and Figure 45. First is based on small pit corrosion. As shown in Figure 46, if two pit corrosion happened, the strain of the left part, the green part shown in Figure 46, will be decreased. Another reason is the temperature influence. The temperature reference FBG has some distance from the three corrosion models, while corrosion is an exothermic reaction. The temperature change caused by corrosion is not removed by equation (4.7), caused the decline in each small cycle shape.

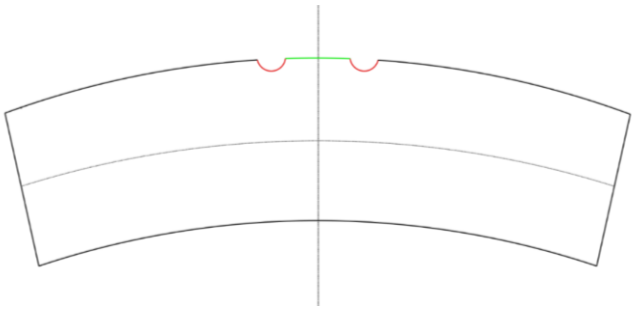

Figure 46 Illustration for two pit corrosion causing strain decline.

Figure 47 shows the results by wiping off the residual strain influence by comparing bending model results with reference 1 and 2. This result fit the theory very well. The rate of strain change should be in direct proportion to corrosion speed and always positive regardless of the FBG embedded position. Figure 47(a), Figure 47(c) and Figure 47(e) show the linear fitting results for every curve. Figure 47(a) shows the best linear relationship. So, this one is considered as our best results. By making average to the left part and right ends of Figure 47(a), through these areas are flat. The curve starts at $-182.238 \pm 1.691\mu\varepsilon$ and ends at $-91.025 \pm 1.467\mu\varepsilon$. So, the total strain change for 600 hours corrosion is $91.213 \pm 3.158\mu\varepsilon$. The average strain change speed is $0.15202 \pm 0.00526\mu\varepsilon/\text{hour}$.

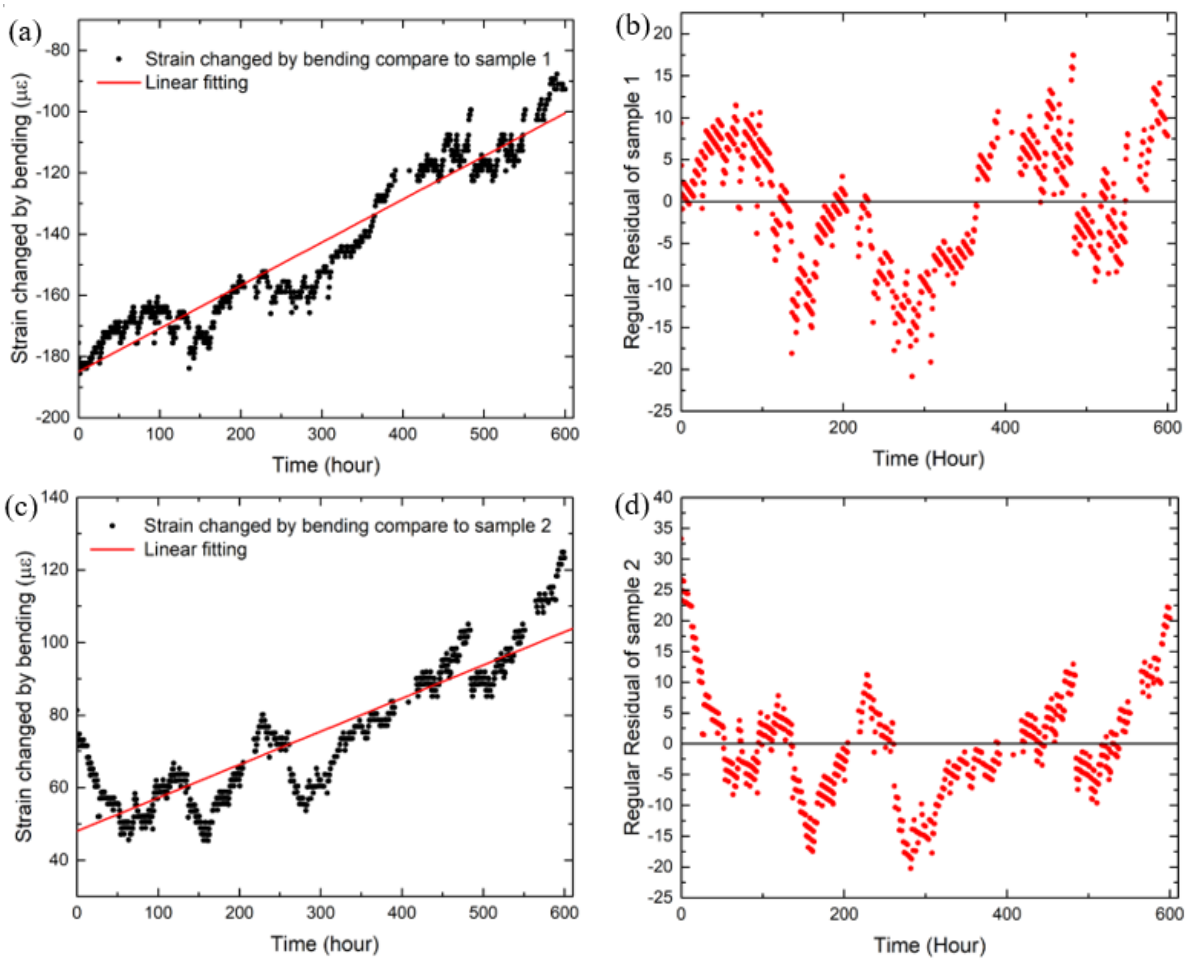

Figure 47 Final results and fitting analysis. (a) Strain changed by bending by comparing bending results to sample 1; (b) Regular residual for linear fitting to sample 1; (c) Strain changed by bending by comparing bending results to sample 2; (d) Regular residual for linear fitting to sample 2

4.4.2.2 Records During Corrosion

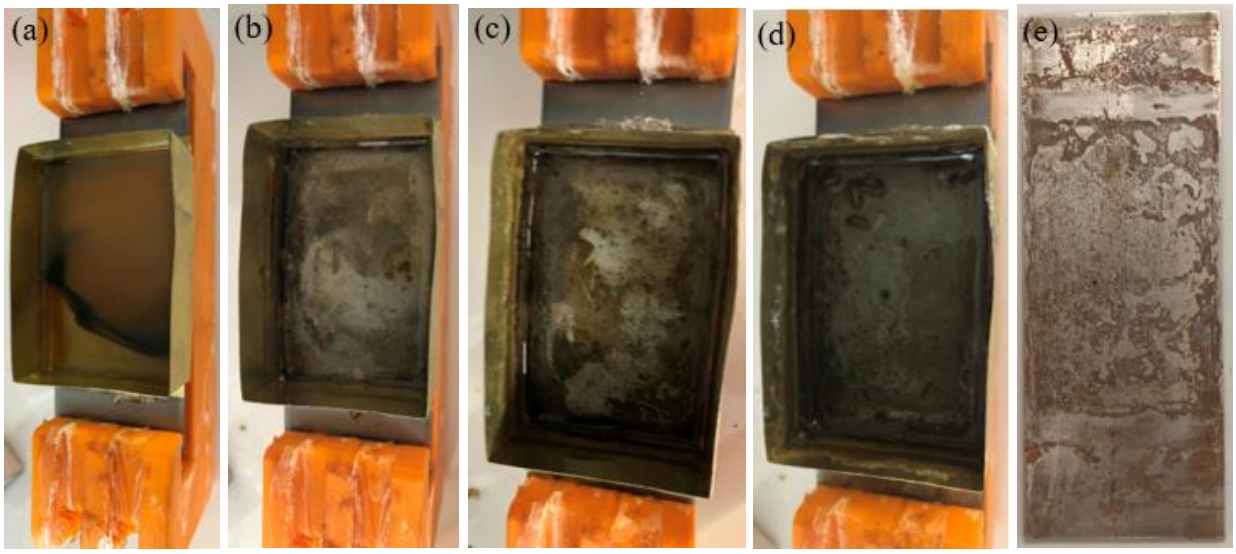

Figure 48 Records for bending model during corrosion. (a) Carbon released during corrosion, the black liquid; (b) 3 days corrosion; (c) 7 days corrosion; (d) 15 days corrosion; (e) After corrosion, the carbon steel surface.

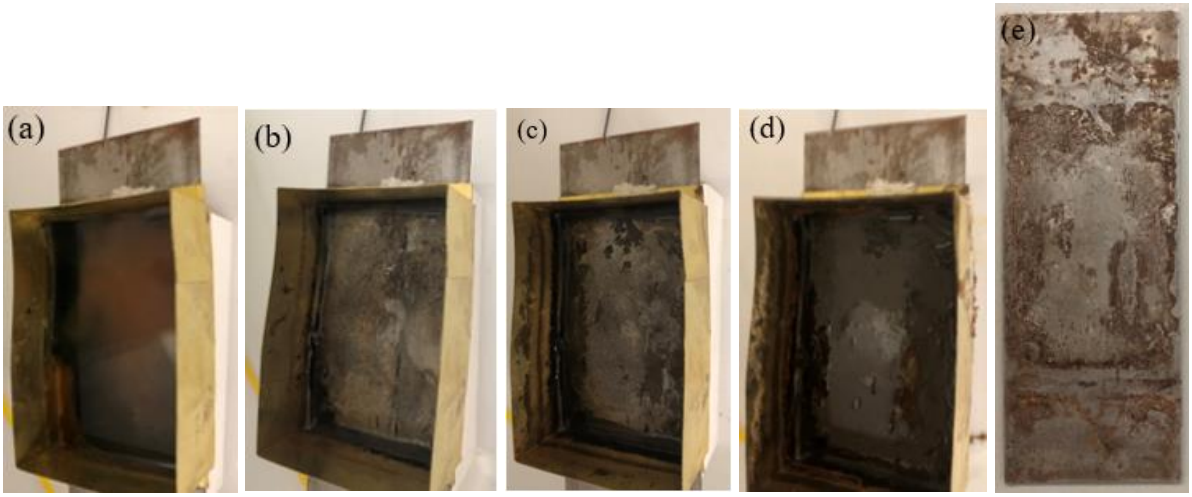

Figure 49 Records for sample 1 during corrosion. (a) Carbon released during corrosion, the black liquid; (b) 3 days corrosion; (c) 7 days corrosion; (d) 15 days corrosion; (e) After corrosion, the carbon steel surface.

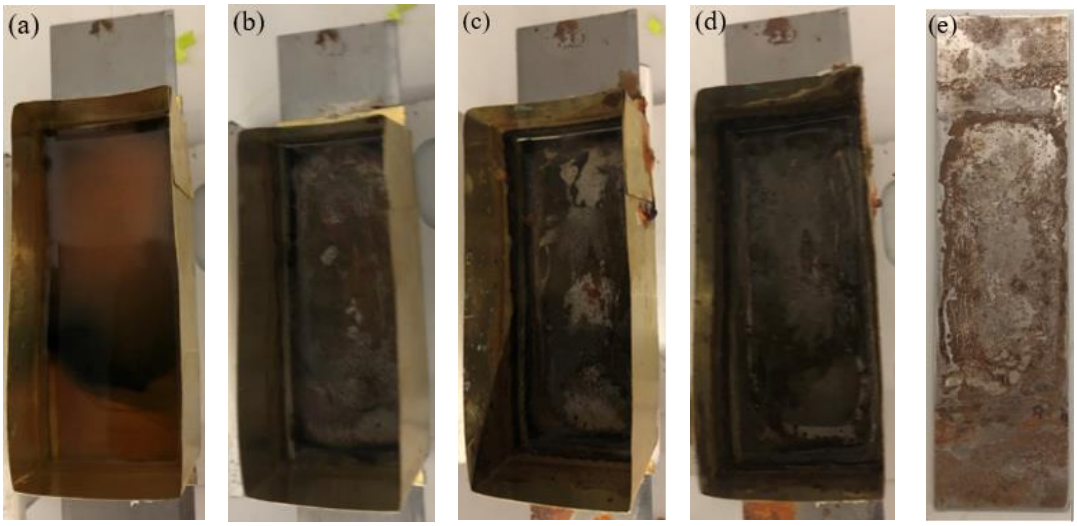

Figure 50 Records for sample 2 during corrosion. (a) Carbon released during corrosion, the black liquid; (b) 3 days corrosion; (c) 7 days corrosion; (d) 15 days corrosion; (e) After corrosion, the carbon steel surface.

Figure 48, Figure 49 and Figure 50 show the records for the corrosion of these carbon steel plates. As shown in Figure 48(a), Figure 49(a) and Figure 50(a), the carbon contained in the carbon steel will be released during corrosion. This is the reason why the 3.5% NaCl solution will be replaced every 3 days. As shown in Figure 48(e), Figure 49(e) and Figure 50(e), the corroded surfaces are not uniform. One reason is that the distribution of impurities in carbon steel is not uniform. The corrosion always first happens at the singular point where it is not pure. Another reason is that the distribution of residual strain is also not homogeneous in the outer layer. The corrosion will first appear at the area where the local strain is big.

Figure 51 Spiral micrometer used for measuring the thickness of the corroded areas.

All the carbon steel plates are 1.59mm in thickness at the beginning. As shown in Figure 48(e), Figure 49(e) and Figure 50(e), the unevenness of bent plate and sample 2 are bigger that sample 1. The thicknesses are measured for each plate after corrosion, as shown in Table 3. For corroded area of bending model, the deep area thickness is $1.4625mm \pm 0.0038mm$ and the shallow area is $1.4772mm \pm 0.0052mm$; For sample 2 are $1.4617mm \pm 0.0084mm$ and $1.4757mm \pm 0.0023mm$. For sample 1, the average thickness is $1.4800mm \pm 0.0029mm$. If consider the average thickness for bending model and sample 2, they are $1.4698mm \pm 0.0088mm$ and $1.4687mm \pm 0.0094mm$. So, the average corrosion speed for bending model is $0.2450 \pm 0.0046\ \mu m/h$; the average corrosion speed for sample 1 is $0.2467 \pm 0.0048\ \mu m/h$; the average corrosion speed for sample 2 is $0.2448 \pm 0.0157\ \mu m/h$. In conclusion, the corrosion speeds are almost same for these three samples. The bending strain at the outer layer has little contribution to the corrosion compared to the residual strain at the outer layer.

Table 3 Thickness of the plates at corroded area.

	Thickness (mm)					
Bending model	1.457	1.466	1.459	1.465	1.466	1.462
	1.475	1.48	1.472	1.471	1.482	1.483
Sample 1	1.473	1.479	1.478	1.482	1.483	1.480
	1.480	1.479	1.485	1.480	1.481	1.480
Sample 2	1.466	1.462	1.445	1.465	1.464	1.468
	1.472	1.479	1.476	1.476	1.476	1.475

Applying equation (2.22), the strain transfer rate is

$$\mathrm{k} = \frac{\varepsilon_m}{\varepsilon_{FBG}} = \frac{1}{893}\frac{v(t)}{\frac{d\varepsilon_{FBG}(t)}{dt}} = 1.4759 \pm 0.0026$$

Then the strain loss due to adhesive layer,

$$\frac{\varepsilon_m - \varepsilon_{FBG}}{\varepsilon_m} = \frac{k-1}{k} = 32.24\% \pm 0.16\%$$

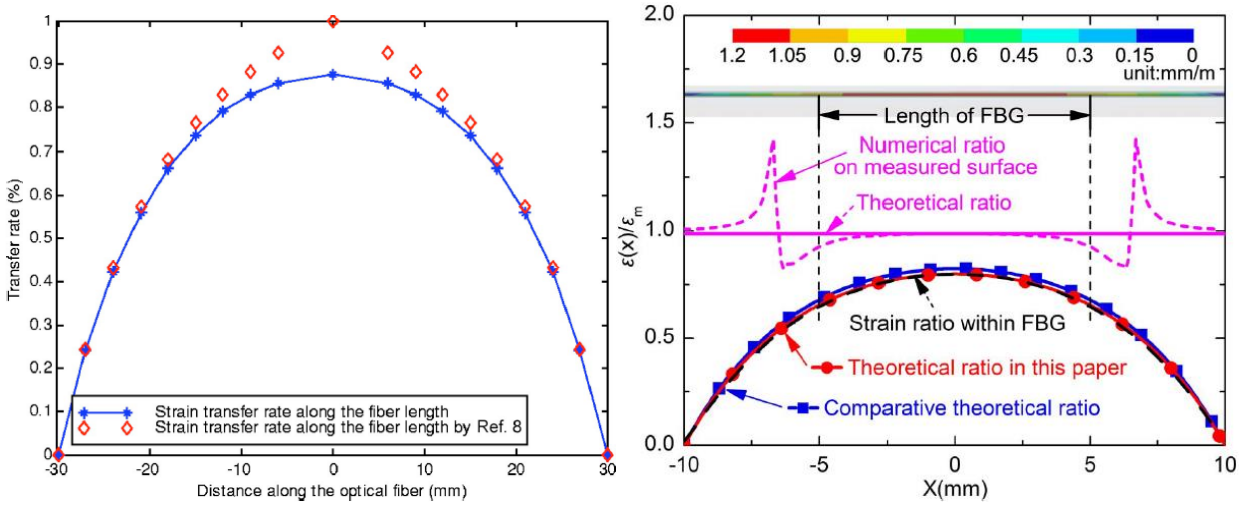

Figure 52 Others' results for the distribution of normal strain in fiber along the length [45], [47]**.**

Figure 52 shows the strain transfer rate $\frac{1-k}{k}$ for others' results. So, our result for a $32.24\% \pm 0.16\%$ strain loss due to adhesive layer is reasonable. The sensitivity for AQ6374 is 0.002nm, and the corresponding sensitivity for strain on FBG is $1.67 \pm 0.01\mu\varepsilon$. After considering the strain loss, the sensitivity for host material (carbon steel plate) is $2.46 \pm 0.03\mu\varepsilon$.

5.0 Conclusion and Future Work

5.1 Conclusion

The average rate of strain change during corrosion for the results is positive during corrosion, fitting the expectation (equation (2.62)) very well. The possible reasons for the decline in each small cycle shape in strain results are local strain loss by two symmetrical small pit corrosion and temperature change caused by corrosion which is not cancelled by the temperature reference FBG in a distance. The sensitivity for AQ6374 is 0.002nm, and the corresponding sensitivity for strain on FBG is $1.67 \pm 0.01\mu\varepsilon$. After considering the strain loss, the sensitivity for host material (carbon steel plate) is $2.46 \pm 0.03\mu\varepsilon$.

5.2 Future Work

5.2.1 A New Four-point Bending Specimen Design

Figure 53 New four-point bending specimen design with much more less material.

Figure 53 shows a new design for four-point bending specimen. When we use the former model, as shown in Figure 31, the fiber needs to be twisted at two sides and requires quite patience to protect bare fiber. Based on this experience, two holes are opened on the two sides of this model, allowing the fiber connectors directly cross though, making the system much easier to install. In order to expand the application condition of the bent corrosion model, several small holes are opened on the bottom plate, designed to be fixed on certain surface using nuts.

5.2.2 Residual Strain Change During Corrosion

For this experiment, because of the time and equipment limitation, we simply consider that the plates made from same process have similar residual strain distribution and scales. The bent influence on corrosion is simply get by making comparation with other samples without bending. But fortunately is that we get the expected results in this way. However, this is just an ideal condition. The residual strain change during corrosion still have a lot of work to deal with it.

5.2.3 Sense the Thickness Change for Multi-layers

From the unexpected results of the carbon steel with adhesive coating, we find that the change of the thickness of the adhesive layer can also be detected, although this change is really small. Such system and method may have potential application in this thickness sense for certain multi-layers.

Bibliography

[1] M. Martins and M. Werneck, *Fiber Bragg Gratings: Theory, Fabrication, and Applications*. Society of Photo-Optical Instrumentation Engineers, 2017.

[2] H. Li, D. Li, and G. Song, "Recent applications of fiber optic sensors to health monitoring in civil engineering," *Eng. Struct.*, vol. 26, no. 11, pp. 1647–1657, 2004.

[3] A. Grillet and D. Kinet, "Optical Fiber Sensors Embedded Into Medical Textiles for Healthcare Monitoring," *IEEE Sens. J.*, vol. 8, no. 7, pp. 1215–1222, 2008.

[4] J. M. Lopez-Higuera and L. R. Cobo, "Fiber Optic Sensors in Structural Health Monitoring," *J. Light. Technol.*, vol. 29, no. 4, pp. 587–608, 2011.

[5] X. W. Ye, Y. H. Su, and J. P. Han, "Structural Health Monitoring of Civil Infrastructure Using Optical Fiber Sensing Technology : A Comprehensive Review," *Sci. World J.*, vol. 2014, 2014.

[6] S.-H. Jo, M. B. G. Jun, H.-E. Joe, and H. Yun, "A review on optical fiber sensors for environmental monitoring," *Int. J. Precis. Eng. Manuf. Technol.*, vol. 5, no. 1, pp. 173–191, 2018.

[7] G. Woyessa, K. Nielsen, A. Stefani, and C. Markos, "Temperature insensitive hysteresis free highly sensitive polymer optical fiber Bragg grating humidity sensor," *Opt. Express*, vol. 24, no. 2, pp. 1206–1213, 2016.

[8] F. Marignetti *et al.*, "Fiber Bragg Grating Sensor for Electric Field Measurement in the End Windings of High-Voltage Electric Machines," *IEEE Trans. Ind. Electron.*, vol. 63, no. 5, pp. 2796–2802, 2016.

[9] A. K. Singh, S. Berggren, Y. Zhu, M. Han, and H. Huang, “Simultaneous strain and temperature measurement using a single fiber Bragg grating embedded in a composite laminate,” *Smart Mater. Struct.*, vol. 26, no. 11, 2017.

[10] Q. Zhang, N. J. Ianno, and M. Han, “Fiber-Optic Refractometer Based on an Etched High-Q π -Phase-Shifted Fiber-Bragg-Grating,” *Sensors*, vol. 13, no. 7, pp. 8827–8834, 2013.

[11] Y. Barbarin *et al.*, “Dynamic high pressure measurements using a Fiber Bragg Grating probe and an arrayed waveguide grating spectrometer,” in *SPIE 9960*, 2016.

[12] S. Sebastian, S. Avvaru, S. S, K. Michael, and S. Asokan, “Hydrostatic Pressure Response of Mo Coated Etched Fiber Bragg Grating Sensor in Side-Hole Packaging,” in *CLEO: Applications and Technology*, 2019.

[13] M. G. Fontana and N. D. Greene, *Corrosion engineering*, Third. New York: McGraw Hill Education Private Limited, 1978.

[14] Ha-Won Song and Velu Saraswathy, “Corrosion Monitoring of Reinforced Concrete Structures - A Review,” *Int. J. Electrochem. Sci.*, vol. 2, no. June, pp. 1–27, 2007.

[15] W. Li, C. Xu, S. C. M. Ho, B. Wang, and G. Song, “Monitoring concrete deterioration due to reinforcement corrosion by integrating acoustic emission and FBG strain measurements,” *Sensors (Switzerland)*, vol. 17, no. 3, pp. 1–12, 2017.

[16] A. Zaki, H. K. Chai, D. G. Aggelis, and N. Alver, “Non-destructive evaluation for corrosion monitoring in concrete: A review and capability of acoustic emission technique,” *Sensors (Switzerland)*, vol. 15, no. 8, pp. 19069–19101, 2015.

[17] C. H. Tan, Y. G. Shee, B. K. Yap, and F. R. M. Adikan, “Fiber Bragg grating based sensing system: Early corrosion detection for structural health monitoring,” *Sensors Actuators, A Phys.*, vol. 246, pp. 123–128, 2016.

[18] C. H. Tan, F. R. Mahamd Adikan, Y. G. Shee, and B. K. Yap, “Non-destructive fiber Bragg grating based sensing system: Early corrosion detection for structural health monitoring,” *Sensors Actuators, A Phys.*, vol. 268, pp. 61–67, 2017.

[19] K. O. Hill, Y. Fujii, D. C. Johnson, and B. S. Kawasaki, “Photosensitivity in optical fiber waveguides: Application to reflection filter fabrication,” *Appl. Phys. Lett.*, vol. 32, no. 10, pp. 647–649, 1978.

[20] G. Meltz, W. W. Morey, and W. H. Glenn, “Formation of Bragg gratings in optical fibers by a transverse holographic method,” *Opt. Lett.*, vol. 14, no. 15, pp. 823–825, 1989.

[21] G. Woyessa, A. Fasano, C. Markos, H. K. Rasmussen, and O. Bang, “Low Loss Polycarbonate Polymer Optical Fiber for High Temperature FBG Humidity Sensing,” *IEEE Photonics Technol. Lett.*, vol. 29, no. 7, pp. 575–578, 2017.

[22] Y. Fu, H. Di, and R. Liu, “Light intensity modulation fiber-optic sensor for curvature measurement,” *Opt. Laser Technol.*, vol. 42, no. 4, pp. 594–599, 2010.

[23] K. S. C. Kuang, W. J. Cantwell, and P. J. Scully, “An evaluation of a novel plastic optical fibre sensor for axial strain and bend measurements,” *Meas. Sci. Technol.*, vol. 13, no. 10, pp. 1523–1534, 2002.

[24] T. Guo, H.-Y. Tam, P. A. Krug, and J. Albert, “Reflective tilted fiber Bragg grating refractometer based on strong cladding to core recoupling,” *Opt. Express*, vol. 17, no. 7, p. 5736, 2009.

[25] Y. ping Miao, B. Liu, and Q. da Zhao, “Refractive index sensor based on measuring the transmission power of tilted fiber Bragg grating,” *Opt. Fiber Technol.*, vol. 15, no. 3, pp. 233–236, 2009.

[26] L. Y. Shao, A. Laronche, M. Smietana, P. Mikulic, W. J. Bock, and J. Albert, “Highly sensitive bend sensor with hybrid long-period and tilted fiber Bragg grating,” *Opt. Commun.*, vol. 283, no. 13, pp. 2690–2694, 2010.

[27] X. Chen, C. Zhang, D. J. Webb, K. Kalli, and G. D. Peng, “Highly sensitive bend sensor based on bragg grating in eccentric core polymer fiber,” *IEEE Photonics Technol. Lett.*, vol. 22, no. 11, pp. 850–852, 2010.

[28] Y.-S. Zhang, Y.-S. Yu, Z.-Y. Zhao, Z.-C. Zhuo, W. Zheng, and Y. Qian, “Bend sensor using an embedded etched fiber Bragg grating,” *Microw. Opt. Technol. Lett.*, vol. 43, no. 5, pp. 414–417, 2004.

[29] Y. G. Han, “Directional bending sensor with temperature insensitivity using a sampled chirped fiber Bragg grating,” *J. Appl. Phys.*, vol. 105, no. 6, pp. 6–10, 2009.

[30] H. J. Patrick, C. Chang, and S. T. Vohra, “Long period fibre gratings for structural bend sensing,” *Electron. Lett.*, vol. 34, no. 18, pp. 1773–1775, 1998.

[31] W. J. Stephen and P. T. Ralph, “Optical fibre long-period grating sensors: characteristics and application,” *Meas. Sci. Technol.*, vol. 14, no. 5, p. R49, 2003.

[32] N. A. M. Eng *et al.*, “Highly sensitive gas refractometers based on optical microfiber modal interferometers operating at dispersion turning point,” *Opt. Express*, vol. 26, no. 22, pp. 29148–29158, 2018.

[33] Raman Kashyap, *Fiber Bragg Gratings*, Second. 2009.

[34] G. Rego, “A Review of Refractometric Sensors Based on Long Period Fibre Gratings,” *Sci. World J.*, vol. 2013, pp. 1–14, 2013.

[35] A. M. Vengsarkar, P. J. Lemaire *et al.*, “Long-period fiber gratings as band-rejection filters,” *J. Light. Technol.*, vol. 14, no. 1, pp. 58–64, 1996.

[36] T. Guo, Á. González-Vila, M. Loyez, and C. Caucheteur, “Plasmonic optical fiber-grating Immunosensing: A review,” *Sensors (Switzerland)*, vol. 17, no. 12, pp. 1–20, 2017.

[37] T. Erdogan and J. E. Sipe, “Tilted fiber phase gratings,” *J. Opt. Soc. Am. A*, vol. 13, no. 2, p. 296, 1996.

[38] T. Guo, F. Liu, B. Guan, and J. Albert, “Optics & Laser Technology [INVITED] Tilted fi ber grating mechanical and biochemical sensors $,” *Opt. Laser Technol.*, vol. 78, pp. 19–33, 2016.

[39] G. Laffon and P. Ferdinand, “Tilted short-period fibre-Bragg-grating-induced coupling to cladding modes for accurate refractometry,” *Meas. Sci. Technol.*, vol. 12, no. 7, pp. 765–770, 2001.

[40] A. D. Kersey, M. A. Davis, H. J. Patrick, M. LeBlanc, and K. P. Koo, “Fiber Grating Sensors,” *J. Light. Technol.*, vol. 15, no. 8, pp. 1442–1463, 1997.

[41] Y. Okabe, R. Tsuji, and N. Takeda, “Application of chirped fiber Bragg grating sensors for identification of crack locations in composites,” *Compos. Part A Appl. Sci. Manuf.*, vol. 35, no. 1, pp. 59–65, 2004.

[42] W. L. Bragg and E. J. Williams, “The effect of thermal agitation on atomic arrangement in alloys,” *Proc. R. Soc. London. Ser. A, Contain. Pap. a Math. Phys. Character*, vol. 145, no. 855, pp. 699–730, 1934.

[43] P. Komarov, Y. T. Chiu, S. M. Chen, and P. Reineker, “Investigation of thermal expansion of polyimide/SiO2 nanocomposites by molecular dynamics simulations,” *Macromol. Theory Simulations*, vol. 19, no. 1, pp. 64–73, 2010.

[44] A. Ghatak and K. Thyagarajan, *Optical electronics*. Cambridge University Press, 1989.

[45] G. Xue, X. Fang, X. Hu, and L. Gong, “Measurement accuracy of FBG used as a surface-bonded strain sensor installed by adhesive,” *Appl. Opt.*, vol. 57, no. 11, p. 2939, 2018.

[46] Anonymous, “G39 Standard Practice for Preparation and Use of Bent-Beam Stress-Corrosion Test Specimens,” 2016.

[47] D. Li, “Strain transferring analysis of fiber Bragg grating sensors,” *Opt. Eng.*, vol. 45, no. 2, p. 024402, 2006.